DOCTORAL SCHOOL IN NATURAL SCIENCES DISSERTATION SERIES
UNIVERSITY OF HELSINKI

LAURI LEHMONEN

QUANTIFICATION OF MRI-DERIVED MYOCARDIAL MOTION IN SPECIFIED CARDIAC DISORDERS

DEPARTMENT OF PHYSICS
FACULTY OF SCIENCE
DOCTORAL PROGRAMME IN MATERIALS RESEARCH AND NANOSCIENCES
UNIVERSITY OF HELSINKI

UNIVERSITY OF HELSINKI
DOCTORAL SCHOOL IN NATURAL SCIENCES DISSERTATION SERIES
6/2020

QUANTIFICATION OF MRI-DERIVED MYOCARDIAL MOTION IN SPECIFIED CARDIAC DISORDERS

Lauri Lehmonen

Department of Physics
Faculty of Science
University of Helsinki

HUS Medical Imaging Center
University of Helsinki and Helsinki University Hospital

Helsinki, Finland

DOCTORAL DISSERTATION

To be presented for public discussion, with the permission of the Faculty of Science of the University of Helsinki, in Auditorium D101, Physicum, Gustaf Hällströmin katu 2, Helsinki, on the 25th of November 2020, at 1 PM.

Helsinki 2020

Supervising Professor:

Professor Sauli Savolainen

Department of Physics
University of Helsinki, Helsinki, Finland
and
HUS Medical Imaging Center
University of Helsinki and Helsinki University Hospital, Helsinki, Finland

Supervisors:

Docent Touko Kaasalainen	Docent Sari Kivistö
HUS Medical Imaging Center, University of Helsinki and Helsinki University Hospital, Helsinki, Finland	HUS Medical Imaging Center, University of Helsinki and Helsinki University Hospital, Helsinki, Finland

Reviewers:

Docent Timo Liimatainen	Docent Mervi Könönen
Research Unit of Medical Imaging, Physics and Technology University of Oulu / Oulu University Hospital, Oulu, Finland	KUH Diagnostic Imaging Center, Department of Applied Physics University of Eastern Finland, Kuopio, Finland

Opponent:

Professor Petro Julkunen

Department of Applied Physics
University of Eastern Finland, Kuopio, Finland
and
Department of Clinical Neurophysiology
Kuopio University Hospital, Kuopio, Finland

ISBN 978-951-51-6833-7 (print)
ISBN 978-951-51-6834 (online)
ISSN 2669-882X (print)
ISSN 2670-2010 (online)

Helsinki 2020

ABSTRACT

Several cardiac diseases affect myocardial function, with local myocardial deformation receiving much attention over the past few years. This work aimed to examine whether globally and locally analyzed quantitative cardiovascular magnetic resonance imaging-derived strain, rotation, and torsion of the heart would bring additional value and deeper understanding to myocardial mechanics in specified cardiovascular disorders. Patients with rheumatoid arthritis, tetralogy of Fallot, hereditary gelsolin amyloidosis, and hypertrophic cardiomyopathy, together with healthy controls, were investigated.

A non-rigid registration-based software solution for myocardial tagging and feature tracking analysis was used for the quantification of left ventricular and right ventricular global and regional strain in different directions. Quantitative motion analysis showed that early treatment of rheumatoid arthritis was useful in retaining the diastolic function of the left ventricle. In adolescents with tetralogy of Fallot, right ventricular circumferential strain was increased relative to healthy controls. Tetralogy of Fallot subjects with increased pulmonary regurgitation had higher right ventricular longitudinal strain than subjects with less pulmonary regurgitation; this has been considered a compensation mechanism. Hereditary gelsolin amyloidosis showed local myocardial changes focused on the basal plane of the left ventricle and differing from the more common light-chain cardiac amyloidosis.

The non-rigid registration-based technique was compared with the harmonic phase-based method with Gabor filtering in the analysis of myocardial tagging-derived rotation and torsion in subjects with hypertrophic cardiomyopathy. The absolute values obtained with the two software methods were significantly different, however, neither software showed significant differences in patients with hypertrophic cardiomyopathy relative to healthy controls. Motion parameters of both ventricles were associated with other quantitative cardiac magnetic resonance imaging parameters, such as volumetric measurements and T1 relaxation times, in the studies of this thesis.

Tagging and feature tracking-derived motion parameters showed significant findings in local myocardial motion in rheumatoid arthritis, tetralogy of Fallot, and hereditary gelsolin amyloidosis. Software-based reference values are required when comparing motion parameters between study subjects. Currently, no standardization for measuring different deformation parameters, such as strain, rotation, or torsion exists, and several software solutions are available for analyzing these parameters. Variability between different software solutions and individual observers should be recognized.

ACKNOWLEDGMENTS

The work towards this thesis took place during 2016–2020 at HUS Medical Imaging Center, University of Helsinki and Helsinki University Hospital. Support from the Doctoral Programme in Materials Research and Nanosciences allowed me to complete this dissertation in a timely manner. The work was financially supported by the State Subsidy for University Hospitals.

I am most grateful to my supervisors, Docent Touko Kaasalainen, for always showing interest in my work, offering valuable help, and reviewing my work, and Docent Sari Kivistö, for providing an optimal environment for conducting research and for her insights into the mechanisms of different cardiac disorders. I am grateful to Professor Sauli Savolainen for his guidance during this thesis and my medical physicist specialization. I offer my sincere gratitude to Docent Miia Holmström for her contributions during the latter half of my thesis; she has been like a supervisor to me, and Docent Kirsi Lauerma, who was the first to introduce me to cardiovascular magnetic resonance imaging.

I thank the official reviewers of my thesis, Docents Timo Liimatainen and Mervi Könönen, who gave valuable feedback and comments on my work on a very tight schedule. I also thank my author-editor Carol Ann Pelli for revising the language of the manuscript.

I am indebted to my coauthors with whom I have had the privilege of working during the past four years. I especially thank Aino-Maija Vuorinen; I began my journey with her, contouring long-axis and short-axis tagging images, and Pekka Ylitalo, my companion in seeking a deeper understanding of myocardial mechanics.

I thank all of my colleagues at the hospital, especially Marjut Timonen and Juha Peltonen, whose expertise in magnetic resonance imaging and cardiac magnetic resonance applications, respectively, is unmatched. I thank Vesa Järvinen for insights into cardiac physiology and for inspiring discussions outside this project. I thank everyone interested in my work during my medical physicist specialization training.

I thank Antti Pekkarinen and Heini Hyvönen for unforgettable moments in Otaniemi with magnetic resonance basics and for continuously tackling new vertical challenges with me.

I am grateful to my family and I warmly thank my parents, Sisko and Ari, for providing a safe haven and always encouraging me to do my best. Finally, I am deeply grateful to Viola for sharing everyday life with me and supporting me in finalizing this project.

Helsinki, November 2020

Lauri Lehmonen

CONTENTS

LIST OF ORIGINAL PUBLICATIONS

This thesis is based on the following publications, which are referred to by their Roman numerals in the text:

I Lehmonen L, Vuorinen A-M, Koivuniemi R, Leirisalo-Repo M, Holmström M, Kivistö S, Kaasalainen T. One-year follow-up study detects myocardial changes with cardiovascular magnetic resonance tagging in active rheumatoid arthritis. *Academic Radiology* 2018; 25:476-85.

II Ylitalo P, Lehmonen L, Lauerma K, Holmström M, Pitkänen-Argillander O, Jokinen E. Severe pulmonary regurgitation in adolescents with tetralogy of Fallot leads to increased longitudinal strain. *Magnetic Resonance Materials in Physics Biology, and Medicine* 2020; 33:309-16.

III Lehmonen L, Kaasalainen T, Atula S, Mustonen T, Holmström M. Myocardial tissue characterization in patients with hereditary gelsolin (AGel) amyloidosis using novel cardiovascular magnetic resonance techniques. *The International Journal of Cardiovascular Imaging* 2019; 35:351-8.

IV Lehmonen L, Jalanko M, Tarkiainen M, Kaasalainen T, Kuusisto J, Lauerma K, Savolainen S. Rotation and torsion of the left ventricle with cardiovascular magnetic resonance tagging: comparison of two analysis methods. *BMC Medical Imaging* 2020; 20:73:1-8.

Study I is reprinted with the permission of Elsevier ©2018, The Association of University Radiologists, published by Elsevier Inc. Studies II-IV are distributed under the terms of the Creative Commons Attribution 4.0 International License (https://creativecommons.org/licenses/by/4.0/) ©The Authors. The results of Study II also appear in the Ph.D. thesis of Pekka Ylitalo.

AUTHOR'S CONTRIBUTION

Study I: The author delineated the ventricular walls in consensus with a radiologist and performed all tagging analyses for left ventricular strain and strain rate with Segment software. The author analyzed the data, performed statistical analysis of the results, and wrote most of the manuscript. The author also revised the final version of the manuscript.

Study II: The author participated in the planning of the study and performed all feature-tracking strain analyses with Segment software. The author also performed the statistical and intra-observer analyses, wrote the methods and results sections, and helped revise the final version of the manuscript.

Study III: The author participated in the planning and image acquisition of the study and performed all segmental tagging, feature-tracking, T1, and extracellular volume analyses with Segment software. The author analyzed the results, performed the statistical analysis, and wrote most of the manuscript.

Study IV: The author planned the study and performed the tagging analysis with Harmonic Phase Flow and Segment software. The author analyzed the results and performed statistical and intra-observer analyses. The author wrote most of the manuscript and revised the final version.

ABBREVIATIONS

2D	two-dimensional
4CH	four-chamber
AHA	American Heart Association
ARP	arrhythmia rejection period
bSFFP	Balanced steady-state free precession
CMR	cardiovascular magnetic resonance
CS	circumferential strain
CSR	circumferential strain rate
ECG	electrocardiogram
ECV	extracellular volume
EF	ejection fraction
FT	feature tracking
HPF	Harmonic Phase Flow
LA	long axis
LGE	late gadolinium enhancement
LS	longitudinal strain
LSR	longitudinal strain rate
LV	left ventricle
MR	magnetic resonance
MRI	magnetic resonance imaging
PR	pulmonary regurgitation
Q1	first quartile
Q3	third quartile
R	Pearson correlation coefficient
RA	rheumatoid arthritis
RF	radiofrequency
RR	subsequent R-peaks in an ECG waveform
RS	radial strain
RSR	radial strain rate
RV	right ventricle
SA	short axis
SPAMM	spatial modulation of magnetization
T1	longitudinal relaxation time constant
T2	transverse relaxation time constant
TE	echo time
TOF	tetralogy of Fallot
TR	repetition time
TSE	turbo spin-echo

1 INTRODUCTION

Many cardiac diseases affect the heart-weakening local myocardial motion, resulting in the investigation of myocardial deformation in recent years. However, accurate assessment of three-dimensional cardiac contraction remains a challenge. Ejection fraction (EF) describes the relative change of myocardial volume between end-systole and end-diastole. EF is the conventional parameter of ventricular function, but is limitated by it being calculated based on volumetric measurements of the ventricles [1]. Myocardial motion-tracking techniques in magnetic resonance imaging (MRI) have been developed for a more accurate description of myocardial deformation than conventional volumetric measurements and EF analysis. Changes in myocardial strain have been detected in subjects with maintained EF, and reports of additional value over EF have been published [2-4]. This has made myocardial deformation analysis popular for research purposes, but methods have only partly attracted clinical interest. Myocardial deformation analysis is mainly performed with cardiovascular magnetic resonance (CMR) imaging or echocardiography-based techniques. Echocardiography is relatively low cost compared with CMR, but suffers from fixed imaging directions and a limited view of different cardiac structures [5, 6]. With CMR, images can be acquired in any direction. Common to both modalities is the observer-related variability in quantitatively derived motion parameters.

In CMR, myocardial deformation imaging has been available since the late 1980s. By modulating magnetization spatially, visually detectable line and grid patterns, referred to as tags, could be created in conventional cine CMR images [7]. The slow acquisition of tagging images and the relatively heavy post-processing have limited applicability to the clinical environment. Several analysis tools have started as research projects and have later been commercialized. In 2009, feature tracking (FT), the quantitative motion analysis of conventional cine image features, was introduced, giving deformation imaging in CMR a boost [8, 9]. Currently, several post-processing software solutions for both tagging and FT are available. The aims of this work were to study CMR tagging and FT-derived global and local deformation parameters in specified cardiac disorders, to relate myocardial motion to other quantitative CMR parameters, and to evaluate reliability of quantitative motion parameters.

2 HEART

2.1 ANATOMY AND FUNCTION

The heart is a muscular organ that rhythmically pumps blood from the low-pressure venous side to high-pressure artery side [10]. The heart consists of four chambers: left and right atria and left and right ventricles. The right atrium receives blood from superior and inferior vena cava, which carry returning de-oxygenated blood from the circulation. Blood flow continues from the right atrium across the tricuspid valve into the right ventricle (RV). Outflow tract of the RV is the pulmonary artery, which transports blood into the lungs. Oxygenated blood returns from the lungs via pulmonary veins and enters the left atrium. Blood then flows across the mitral valve into the left ventricle (LV). The LV has a thick muscular wall, allowing the generation of high pressures during LV contraction [11]. The LV is responsible for ejecting blood across the aortic valve into the aorta. The pumping activity of the heart is commonly expressed in terms of cardiac output, the amount of blood ejected with each contraction.

The heart is constantly moving, from diastole to systole. At the end of diastole, the heart is momentarily still before the next cardiac cycle. The motion of the heart is controlled by an electric conduction system, where each heartbeat originates from an electrical impulse induced by the sinus node located in the right atrium [12]. The impulse first causes the atria to contract, pushing more blood into the ventricles. The impulse then spreads to both ventricles, causing their synchronous contraction. The cardiac cycle displayed in a Wiggers diagram (Figure 1) visualizes the change in LV volume in relation to an electrocardiogram (ECG) signal during a single heartbeat [13].

The cardiac cycle is divided into two periods: systole and diastole. Systole refers to ventricular contraction and ejection, while diastole refers to the rest of the cardiac cycle, including ventricular relaxation and filling [12]. The P wave represents the depolarization of the atria, finishing the diastolic phase of the heart. Following the P wave, the QRS complex, representing the depolarization of the ventricles, first spreads around both ventricles and then causes both ventricles to contract. The QRS complex begins the systolic phase, and during ventricular contraction the volume of the ventricles decreases to a minimum. During systole the T wave of the ECG represents repolarization of the ventricles. When the ventricular volumes are at a minimum, pressure in the ventricles drops. Atrioventricular valves open, beginning the diastolic filling of both ventricles and consequently increasing the volume of both ventricles. The diastole ends with the next P wave, finalizing the filling of both ventricles before the next contraction.

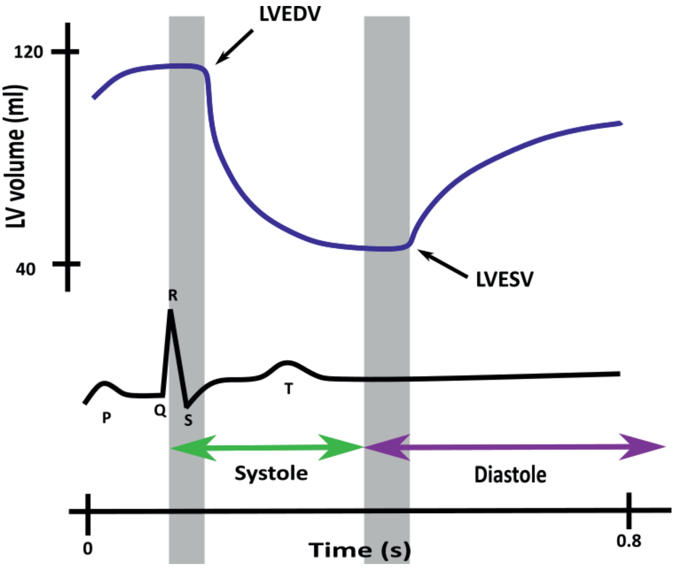

Figure 1: A Wiggers diagram, the classic illustration of the cardiac cycle. The diagram links different cardiac phases to left-ventricular volume and an electrocardiogram signal. The gray columns at the beginning of systole and diastole denote isovolumetric contraction and relaxation of the LV, respectively. LVEDV = left-ventricular end-diastolic volume, LVESV = left-ventricular end-systolic volume.

2.2 NOMENCLATURE AND LEFT VENTRICLE SEGMENTATION

CMR, echocardiography, nuclear medicine, and computed tomography are imaging modalities that have been used to measure LV function for clinical diagnosis and research purposes [14]. The technical principles of these modalities are different; however, they all image the cardiac muscle. Several factors, such as the orientation of the heart, angle of cardiac planes, and slice thickness of the chosen modality, have evolved independently within each modality. This has resulted in a lack of standardization and made intra- and inter-modality comparison difficult. The American Heart Association (AHA) has created a standardized 17-segment model in 2002 for the segmentation and nomenclature of the LV to allow repeatable characterization of LV function between modalities [15]. The AHA recommendations state that the definition, orientation, and display of the heart should be done using the long axis (LA) of the LV and planes oriented perpendicular relative to the LA. Names of these planes should be short axis (SA) view, horizontal LA, and vertical LA. These LA views correspond to four-chamber (4CH) and three-chamber views, respectively, common in CMR.

The LV muscle can be divided into various numbers of segments. The number of segments depends on the method employed. For example, CMR and computed tomography have included up to 48 segments, far exceeding clinical need [16]. The AHA 17-segment model is based on autopsy data to section the heart into apical, mid-ventricular, and basal thirds perpendicular to the LV LA. The sectioning creates a mass distribution of 35%, 35%, and 30% for basal, mid-ventricular, and apical planes, respectively, closely matching ventricular mass distribution of the autopsy data [17]. The segment system was primarily developed for the analysis of regional wall motion of the LV, but the segment for the myocardial apex was added as the assessment of myocardial perfusion became viable, rendering a 17-segment model. Due to complex mixing of the myocardium and connecting tissue, specifically at the base of the heart, SA images of basal, mid-ventricular, and apical planes should be selected to include myocardium in all 360° locations [15]. The 17th segment, the apex, can be evaluated from LA planes. Anatomic landmarks should be used when selecting these slices.

According to AHA, the naming of individual segments should be done with reference to both the LA of the ventricle and the 360° circumferential locations on SA views. *Basal*, *mid-ventricular,* and *apical* are parts of the names and define the LA location of the SA segments. The circumferential location, in basal and mid-ventricular slices, should be divided into six segments of 60° each. The attachment of RV wall to the LV should be used to separate the septum from LV anterior and inferior free walls [15]. A bull's eye plot showing the location and naming of the 17 segments is displayed in Figure 2. The numbering of the segments starts from the basal anterior segment and runs counterclockwise around the heart, continuing to the mid-ventricular plane.

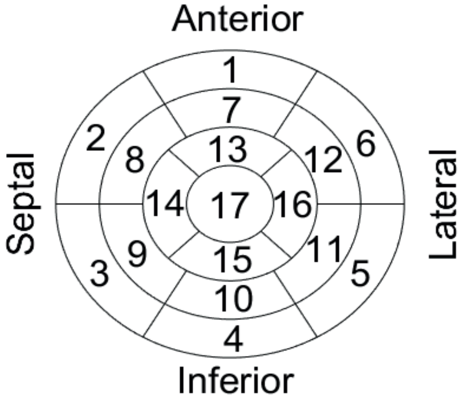

Figure 2: The 17-segment model of the American Heart Association. The numbering of the segments starts from the basal anterior segment (segment 1) and runs counterclockwise around the heart to the basal anterolateral segment (segment 6), continuing to the mid-ventricular plane.

The three SA levels of the LV present different shape and motion properties [18]. The basal plane undergoes plane motion during the cardiac cycle with a fixed image plane, while this kind of motion is almost non-existent in the apical plane. The apical and basal planes both cause a significant rotating motion, while the mid-ventricular plane is mainly dominated by radial contraction. This makes local motion analysis in different cardiac planes and directions viable.

2.3 COMPONENTS OF MYOCARDIAL MOTION

Strain is a measure of the relative contraction in a given direction of the cardiac muscle. Myocardial strain in CMR is commonly referred to as Lagrangian strain since the myocardium moves as a continuous mass rather than a discrete material point [8, 19]. Myocardial Lagrangian strain as a function of time t is defined as follows [20]:

$$\text{strain}(t) = \frac{L_t - L_0}{L_0} * 100\% \,, \tag{1}$$

where L_0 is the measured length of the myocardium at time point zero and L_t the length at time t. Strain is expressed as a percentage and commonly measured in circumferential, longitudinal, and radial directions of the LV, starting from end-diastole as time point zero. This is when the ventricle is filled with blood and the myocardium is relaxed.

Strain can be measured in SA and LA directions of both ventricles, based on epicardial, endocardial, or mid-myocardial contours; mid-myocardial being the conventional one in CMR. Circumferential and radial strain can be measured from SA images of the LV. In the LA direction, longitudinal strain can be measured in both ventricles. The ventricular wall of the RV is much thinner than that of the LV, and thus, radial strain can only reliably be measured in the LV [21]. The relaxed state of end-diastole is the reference point for strain analysis, thus, negative strain indicates myocardial thinning or shortening, whereas positive strain indicates thickening or lengthening. Strain rate is the time derivative, the rate of change of the strain curve. Strain rate is highest when strain is changing most rapidly in the least amount of time. Accordingly, strain rate is zero at maximum strain. Peak values for strain, systolic strain rate, and diastolic strain rate are all clearly visualized as peaks in strain and strain rate curves (Figure 3). Strain curves can be calculated as a mean in different cardiac planes or segmentally. Peak strain is calculated either as a mean value of the peak values of different segments or as a peak of the entire contour in the plane of analysis.

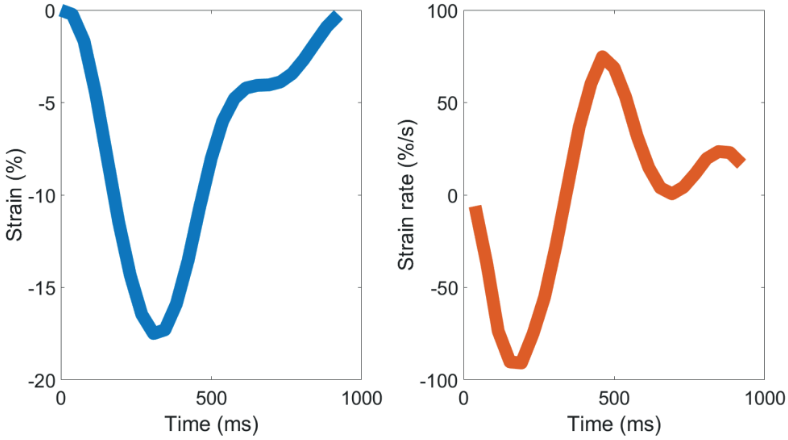

Figure 3: Curves demonstrating mid-LV circumferential strain (left) and corresponding strain rate (right). At the time of peak strain, strain rate is zero. When strain rate is at its minima or maxima, strain is changing the most in the least amount of time.

Common definitions for strain include global strain and planar strain; however, segmental strain is gaining wider interest as more post-processing tools become available. Comparison of strain values between subjects is performed by comparing numerical peak strain values [22-25]. Comparison of strain curves is more complicated due to different lengths of RR intervals between subjects.

Time resolution affects measured strain and strain rate. Cine images can be considered as sampling points of a signal, in this case the strain curve. If the time between consecutive sampling points is large relative to the entire duration of a cardiac cycle, the shape of the curve is deformed. In the literature, the minimum number of cine image phases for strain rate analysis should be at least 25 [26]. At a heart rate of 60 beats per minute, a time resolution of 40 ms is obtained.

Although strain is the most studied parameter with CMR, the wringing motion of the heart is also of interest [27]. Left-ventricular rotation, measured in degrees, and torsion are relevant when investigating the effects of different cardiovascular diseases on myocardial motion. Rotation is defined as the angular displacement of the LV about its central axis in SA direction, measured from end-diastole. When looking at the heart from the apex during systole, the basal SA plane of the LV rotates clockwise, while the apical SA plane rotates counterclockwise [28]. Peak rotation is reached at end-systole, when the heart is most contracted. In diastole, the rotation pattern is reversed. Torsion, in its simplest form, also referred to as twist, is defined as the rotational difference between apical and basal planes. Torsion as a function of time is as follows [29]:

$$T(t) = R_A(t) - R_B(t), \tag{2}$$

where $R_A(t)$ and $R_B(t)$ are the counterclockwise rotation of apical and clockwise rotation basal planes, respectively. Torsion reaches its maximum value at end-systole, when the rotational difference between apical and basal plane is the highest. The torsion definition of equation (2) is absolute and it doesn't acknowledge the size of individual hearts. Other definitions of torsion utilize the longitudinal distance and myocardial wall thickness to normalize torsion values of different-sized hearts [27].

3 MOTION ANALYSIS IN CARDIOVASCULAR MAGNETIC RESONANCE IMAGING

3.1 BASICS OF MAGNETIC RESONANCE IMAGING

The signal in MRI is generated by the interaction of applied magnetic fields with hydrogen atoms (protons) inside the human body. Hydrogen nuclei are spin $^1/_2$ particles, which results in them having a magnetic moment [30]. Due to the magnetic moment, when experiencing an external magnetic field, the hydrogen nuclei align themselves either parallel or anti-parallel to the field. A slight majority of the nuclei will align parallel to the field, due to the lower energy state, which results in a net longitudinal magnetization along the external magnetic field. This net magnetization is the vector sum of magnetic moments from many individual hydrogen nuclei and its magnitude is extremely small relative to the external field [31]. The hydrogen nuclei will precess about the external magnetic field at a frequency depending on the magnitude of the magnetic and gyromagnetic ratio of the nuclei. Applying a radio frequency (RF) pulse oscillating at the same frequency, the net magnetization vector sum can be tipped away from the direction of the external field. This is a requirement to measure a detectable signal from the hydrogen inside the body. When the RF pulse is terminated, the net magnetization, now perpendicular to the external magnetic field, will return to equilibrium, by the hydrogen nuclei releasing energy to the environment. Before the net magnetization has fully recovered, the precessing magnetization can be detected using a RF receiver coil. The recovery of net magnetization, termed relaxation, is characterized by spin-lattice (T1) and spin-spin (T2) relaxation time constants. The signal available from tissue is determined by several factors, including MRI sequence parameters, proton density, and T1 and T2 relaxation times [32]. The contribution of T1 and T2 relaxations along with proton density to image appearance is controlled through the manipulation of pulse sequence parameters. In the simplest example of an MRI signal, an RF pulse of 90° is applied to rotate the net longitudinal magnetization perpendicular to the magnetic field of the MRI scanner. It will then result in a signal that can be detected with an RF receiver coil. This signal is called the free induction decay, as it gradually decays due to relaxation. The free induction decay in practice is not used for MR image acquisition. However, a sequence of RF pulses in combination with MR field gradients is used to generate echo signals that are recorded with RF receiver coils and reconstructed to yield an MR image.

Specific magnetic field gradients are used for MRI slice selection, spatial encoding in phase encoding direction and frequency encoding direction, and signal readout. This process effectively only excites hydrogen nuclei within a small volume, a single slice, and codes the spatial position of the excited hydrogen nuclei based on frequency and phase. When the MR signal is sampled as spatial frequency data with a receiver coil, it will be arranged in digital format in a two-dimensional data matrix. Low spatial frequency data fill the central area of the matrix, providing information about the general shapes and contrast in the resulting image, while high spatial frequencies at the periphery represent image resolution and detail [33]. MR images are formed by applying a two-dimensional Fourier transform to the spatial frequency data row by row and column by column. This process decodes the spatial position of the hydrogen nuclei based on variations in frequency and phase. During the reconstruction process a relative signal intensity value is assigned for each image voxel based on the strength of the signal in the corresponding tissue volume. The resulting MR image illustrates anatomical relationships and grayscale contrast between tissues based on magnetization behavior in the given slice of tissue [34].

3.2 SPECIFICS OF CARDIOVASCULAR MAGNETIC RESONANCE

CMR imaging has been considered difficult to perform due to many technical challenges that arise from the heart itself [35]. These are mainly cardiac motion, respiratory motion and pulsating blood flow [36]. All of these cause changes in MR signal intensity or phase with time and typically result in ghosting artifacts. CMR imaging involves the imaging of a constantly moving target, which sets high technical requirements for imaging hardware. Most CMR images cannot be acquired quickly enough to avoid cardiac motion but the motion can be effectively negated by gating or triggering image acquisition to cardiac physiology.

The electrical signals of the heart can be measured with an ECG during CMR imaging, which is the most common method in clinical CMR use. ECG gating is required to ascertain the exact position of the heart, and recording a proper ECG signal is crucial for successful cardiac gating and successful image acquisition [37]. Gating is used so that imaging data are systematically acquired at the same point in the cardiac cycle; ideally the heart is also in the same position between the cycles. Acquiring a good ECG signal inside the bore of the MR system is not trivial for two important reasons: 1) the ECG electrodes need to be placed relatively close to each other to avoid large voltages being induced by the gradient and radiofrequency coils; 2) the ECG waveform is distorted due to a magneto-hydrodynamic effect, which is caused by a moving conducting fluid (blood) inside a magnetic field [38]. Blood flow in the aorta occurs at the same time as ventricular ejection and the repolarization of the ventricles, which causes an additional voltage on the T wave of the ECG. This may sometimes increase the amplitude of the T wave over the amplitude of the R wave and result in incorrect triggering of the CMR acquisition [39, 40]. The use of vector cardiac gating has made triggering much more reliable. With vector cardiographic gating, left-to-right and superior-to-inferior components of ECG are acquired simultaneously, minimizing the magneto-hydrodynamic effect and the incorrect T wave triggering [41].

In addition to cardiac motion, respiratory motion also affects the location of the heart. The heart is located directly above the diaphragm and inhalation and exhalation both affect its location. The simplest solution is to acquire images entirely during breath-hold, during multiple heartbeats with a single phase-encoding step during each heartbeat. Sequences that are not fast enough to be acquired during a single breath-hold are divided into multiple breath-holds. To achieve shorter acquisition times, fast imaging techniques acquire more than one phase-encoding step per heartbeat [42]. This way the phase-encoding data is sampled much quicker, leading to shorter acquisition time. Spin-echo sequences that use this sort of principle are known as turbo spin-echo (TSE) sequences. Echo planar imaging is a form of single-shot pulse sequence, which can acquire all phase-encoding data with a single RF excitation and readout. Echo planar imaging has limitations related to generally low spatial resolution and artifacts due to phase inconsistencies, making it suboptimal in CMR [43].

CMR can be used to acquire still morphological images, which provide valuable information about subject anatomy. With TSE sequences, morphological images can be acquired during a single breath-hold [44]. These images are described as black-blood or dark-blood images due to their nature of minimized signal originating from the blood. With TSE technique, the echo train length can be relatively long, which is why the echoes are collected in diastole when the heart is momentarily still. Blood inside the cardiac chambers is also still and to overcome the undesirable signal of the blood, double inversion recovery schemes are used before the TSE acquisition [45]. The main principle of the double inversion recovery is to start with a non-selective 180° inversion pulse, immediately followed by a slice-selective 180° inversion. This scheme inverts all magnetization outside the imaging volume, while magnetization within the image slice is effectively unchanged. A short inversion time after the double inversion will cause de-inverted blood within the image slice to wash out and be replaced by inverted blood, which will recover according to T1 relaxation. Inversion time is chosen so that at the time of TSE readout the inverted blood gives minimal signal [46]. If all blood is replaced during the inversion time, proper black-blood images will be acquired. However, slow-flowing blood or blood flow that occurs in-plane may not be fully suppressed [47].

The imaging planes of CMR do not typically represent the axial, sagittal, and coronal views of the body. CMR planes are conventionally orientated to the ventricular chambers and valves. Obtaining the standard CMR views requires knowledge of cardiac anatomy and much practice [48]. MRI systems can acquire thin, less than 1-mm-thick slices. In CMR, however, the conventional images are 6-10 mm thick, as there is no clear benefit of very thin slices. Rather, thin slices may cause trouble with lower signal-to-noise ratios [49].

3.3 SEQUENCES FOR CAPTURING MYOCARDIAL MOTION

The most common application of CMR is the use of vector cardiographic gated gradient-echo-type sequences designed to visualize the heart's motion throughout the cardiac cycle [50]. This is termed functional imaging, but it should not be confused with functional magnetic resonance imaging of the brain. Gradient-echo sequences have very short repetition times (TR), making them suitable for acquiring images at the same anatomical location at distinct points in the cardiac cycle. Balanced steady-state free precession (bSSFP) is a gradient-echo sequence designed to ensure that the transverse magnetization is brought back into phase at the end of each TR when the next RF pulse is applied. This carries over into the next repetition and is superimposed with transverse magnetization created by that RF pulse. After multiple repetitions, a steady-state condition is achieved, where the transversal magnetization of multiple TRs combine to give much greater signal [50]. SSFP is the most used sequence type for creating functional CMR images, that is, still images of different cardiac planes at different points in time. Each still image represents a temporal phase of the cardiac cycle. The still bSSFP images are presented as cine image stacks, which visually present the heart contracting and relaxing. The contrast in bSSFP images is mainly dependent on the relaxation time ratio T2/T1, making fluids and fat appear bright [51]. The ratio is high in blood and lower in the myocardium, therefore, bSSFP images are insensitive to flow and offer excellent contrast between the myocardium and blood [52]. In the case of a non-uniform magnetic field, transverse magnetization from different TRs can cancel out rather than add together in inhomogeneous areas, introducing dark banding artifacts across bSSFP images [53].

Ideally, data of each cine image would be acquired during a single breath-hold. However, each cine image involves the acquisition of several phase-encoding steps, like echo train length in TSE. The technique of acquiring several phase-encoding steps in a single RR interval of the ECG is termed segmented k-space imaging [54]. The idea is to acquire phase-encoding steps for several cine views during the same RR interval. This way a single breath-hold is enough to acquire all of the phase-encoding steps needed for a cine image series. Since the duration of image acquisition is dependent on the number of RR intervals, patients with a faster heart rate need to hold their breath for a shorter period of time.

Cine images can be acquired either with prospectively or retrospectively gating the ECG signal. Many people have arrhythmias that vary the heart rate. This is problematic from the image acquisition point of view. Any heartbeat that is shorter than normal (at the start of the scan) will result in incomplete data acquisition. The changing heart rate can be handled by using prospective cardiac gating. This way, an arrhythmia rejection period (ARP) is set around each R peak in the ECG. The ARP is typically around 15% of the RR interval. During the ARP image acquisition is disabled to account for the varying heart rate. The pulse sequence continues to run though in order to keep the magnetization in a steady state. This prospective gating looks for the next R peak after ARP to occur. All data that are acquired when an RR interval falls outside the ARP are discarded and need to be reacquired. The clear disadvantage of prospective cardiac gating is that due to the ARP important ventricular motion information during late diastole is missed [50, 55].

Alternatively, cine image data can be acquired throughout the cardiac cycle, the ARP included. The duration of each heartbeat is recorded. Any variation in the RR interval is addressed by retrospective processing, hence, the name retrospective cardiac gating [56]. After completing the scan, every heartbeat is either stretched or compressed to match the nominal RR interval. The time point of each phase-encoding step is reassigned. The acquired data are retrospectively allocated to a user-defined number of temporal phases. A typical approach for allocating acquired temporal phases to user-defined temporal phases is the nearest neighbor algorithm. The relative acquisition time of each phase-encoding step may not be the same, which is why it may be necessary to use the same phase-encoding step in adjacent user-defined temporal phases. The reconstruction engine ensures the full sampling of the cardiac cycle. Retrospective gating commonly also uses the ARP; however, it is much larger, even 50% of the average RR interval. This way, only very short or very long heartbeats are being rejected [38]. Cine images are acquired during many heartbeats, and although they showcase the heart contracting and relaxing, they should not be thought of as real-time visualization of the cardiac cycle, but as averages of multiple heartbeats.

Cine CMR is a great tool for visual analysis of general myocardial motion. However, even with post-processing tools cine images do not provide information on myocardial motion inside the myocardial wall, as the cardiac muscle is homogeneous in cine images. Myocardial tagging is a special CMR technique, which refers to marking the cardiac muscle non-invasively. Tagging can be described as a process of producing saturated planes that are orthogonal to the imaging plane. The technique was created in the late 1980s by Zerhouni et al. [7], which allowed for the first time the visualization of intramural myocardial motion without the use of invasive myocardial markers. During the past decades numerous improvements have been made, and several different techniques are nowadays available [57-59]. A technique initially created by Axel and Dougherty is still widely used today [60]. The creation of the tagging pattern is achieved with spatial modulation of magnetization (SPAMM), where saturation pulses are used for creating stripe or grid patterns in conventional cine CMR images (Figure 4).

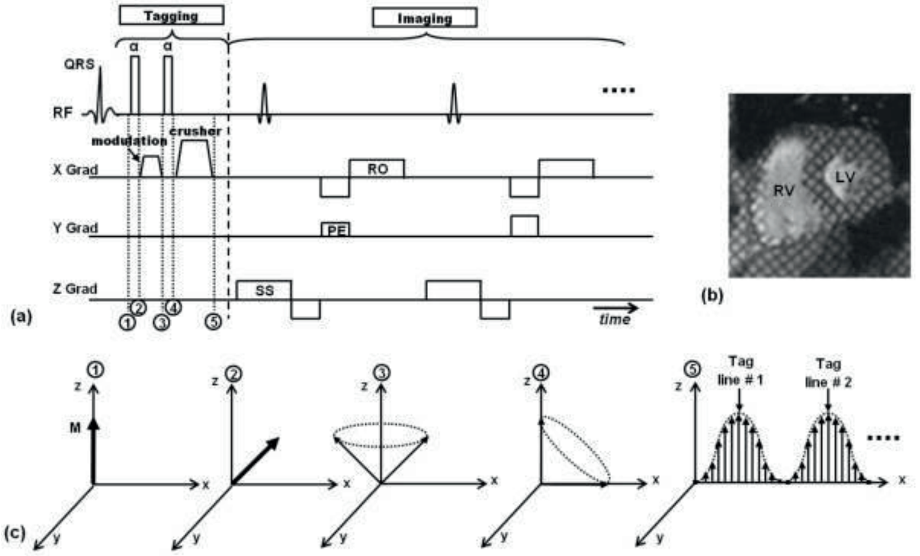

Figure 4: a) The original spatial modulation of magnetization tagging pulse sequence. The tagging part has two non-selective RF pulses that are separated by a tagging gradient in the tagging direction and followed by a crusher gradient. The imaging part shows conventional k space acquisition with slice-selection (SS), phase-encoding (PE), and read-out (RO). This kind of sequence creates parallel tag lines that are orthogonal to the x-axis. b) Example of grid tag pattern, c) Evolution of net magnetization during different phases in the tagging part of the sequence. Adopted from Ibrahim [61].

SPAMM is based on wrapping magnetization periodically through space with two equal non-selective RF pulses that are separated by a wrapping gradient [61]. The first RF pulse flips the magnetization in the transversal direction (Figure 4 c). A gradient pulse is immediately applied in the desired tagging direction, which modulates the transversal magnetization in a sinusoidal fashion. The modulated magnetization is then flipped back to the starting position by another RF pulse. A large spoiler gradient follows the second RF pulse, eliminating possible remaining transversal magnetization. This kind of scheme creates tagging lines in one direction. When grid tagging is required, a second tagging scheme follows with the modulating gradient oriented orthogonally compared with that of the first tagging scheme. Image acquisition then follows at the desired time to visualize tissue deformation. The image acquisition phase is separate from the tagging phase and the tagging pattern deforms based on tissue movement between the phases. SPAMM was the sequence that made tagging possible in routine CMR examinations. The use of SPAMM tagging in motion tracking has been later validated by phantom studies [62, 63]. The sequence in Figure 4 is the original sequence and later developments have implemented tagging schemes to conventional bSSFP cine image acquisition.

SPAMM tagging sequences today provide high spatial resolution and high temporal resolution. After the tagging phase, the tagged magnetization is exponentially relaxing back to equilibrium state according to T1 relaxation. The longer the time between the tagging phase and imaging phase, the poorer the contrast between tag lines and non-tagged tissue will be. This is why the tagging pattern tends to fade in late diastole, making motion assessment more difficult. The fading can be minimized by using low flip angles for the bSSFP imaging part of the sequence [64]. The magnetic field strength of the MR system also affects the tagging pattern. Using a 3T MR system, the signal-to-noise ratio is theoretically doubled compared with 1.5T systems and T1 relaxation is prolonged [65]. The prolonged T1 relaxation means a longer time before the tagging pattern begins to fade.

Myocardial tagging has been employed in measuring regional LV function, contractility, rotation and torsion, aging, coronary artery disease, among others [61, 66-69], however, lack of fast quantitative analysis tools is preventing CMR tagging from being widely adopted in clinical use. Most software solutions utilize image processing techniques to detect tag features to create detailed displacement maps [70].

3.4 MOTION QUANTIFICATION

3.4.1 MYOCARDIAL TAGGING

The general principle of motion analysis techniques is that they search patterns of features in CMR images and follow them from one image frame to the next, analyzing the most probable correspondence. A number of technical solutions have been proposed for the semi-automated extraction of myocardial deformation from CMR tagging images. Possible methods include optical flow [71-73], harmonic phase (HARP)[74, 75], spline snake grids [76], and non-rigid registration based on free-form deformation [77, 78]. Different methods can be roughly divided between those that work in frequency space and employ spectral methods to estimate tag motion and those that work in the spatial domain and consider tagging lines as features to track.

Harmonic Phase Flow (HPF) plugin (Computer Vision Center, Barcelona, Spain) [28, 79, 80] is a HARP-based analysis algorithm that employs a variational Gabor filter bank to extract myocardial displacement information. In HARP, the intensity of the tagged MR image is expressed in complex form in Fourier space. The phase of these so-called harmonic images are only a material quantity and as such remain constant over time. This is why they can be used to follow the location of the tagging pattern throughout the cardiac cycle.

SPAMM tagging patterns are generated by applying a sequence of N RF pulses over a short time interval. The simplest case of 1-1 SPAMM tagging has only two RF pulses. Axel and Doherty proposed the use of a binomial combination of RF pulses in the tagging phase [64]. The higher the binomial order grows, the sharper the tagging lines [61]. A one-dimensional tagging pattern generated with N RF pulses has $2N-1$ spectral peaks in the Fourier domain; correspondingly, a two-dimensional (2D) pattern is a product of two one-dimensional patterns and has $(2N-1)^2$ spectral peaks [75].

A 2D SPAMM tagging sequence with two main frequencies (ω_1, ω_2) produces $K = (2N-1)^2$ spectral harmonic peaks in the frequency domain. The number of these peaks depends on the number of RF pulses applied to produce the pattern [75]. From this follows that any tagged image frame $I(x,y;t)$ can be expressed as a composition of complex harmonic images I_k [28]:

$$I(x,y;t) = \sum_{k=1}^{K} I_k(x,y;t) = \sum_{k=1}^{K} I_0\big(p(x,y;t)\big)c_k(t)e^{i\langle\omega_k,p(x,y;t)\rangle}\,, \qquad (3)$$

where $p(x,y;t)$ is a reference map that relates a point (x,y) at time t to its associated material point at $t = 0$, I_0 is the underlying CMR image without tags, and c_k is a function modeling tag fading. The term inside the scalar product $\langle\,,\rangle$ is the phase of each HARP image, which is a stable tissue property. The equation shows that the SPAMM tagged image is a sum of K complex images, referred to as harmonic images. Each harmonic image corresponds to a distinct spectral peak identified by frequency ω_k. As harmonic images are complex, they have both magnitude and phase. The phase $\Phi_\mathrm{k}(x,y;t) = \langle\omega_k, p(x,y;t)\rangle$ of each harmonic image is given by the exponent term, and it is linearly dependent on the reference map $p(x,y;t)$ [28]. The phase remains constant despite intensity variations and fading of the tagging pattern. The phase, which takes its values in the whole real line, cannot be in practice properly retrieved, instead the principal wrapped value defined $[-\pi,\pi[$ is used [74, 81]. This calculated phase of a harmonic image is referred to as a HARP image. Two HARP images with independent spectral peaks are required to obtain 2D information. This means a one-dimensional tagging pattern is only capable of extracting one-dimensional information.

The analysis of HARP images for myocardial deformation is an image processing problem and is affected by image quality. HARP tracking estimates tissue motion assuming a material point at time t must have the same harmonic peak values at time $t + 1$ due to phase constancy [74]. When a tagged image is acquired, all harmonic images I_k are mixed and in order to separate them some form of filtering is required. Several solutions have been proposed such as elliptical band-pass filters [75] and Gabor filters [82]. Gabor filters are linear filters used in texture analysis; they analyze whether specific frequency content is around a region of interest in specific directions in an image. Their potential lies in the fact that they have tunable parameters to offer accurate representation of HARP images.

HPF solves the HARP tracking problem using a Gabor filter bank in an alternative mathematical framework. To obtain the phase images Φ_k, the computation of harmonic images I_k is first required. In the case of 2D grid tagging pattern, band.pass Gabor filters centered at main spectral peaks $\omega_k$will be sufficient. The best results will be obtained when variable filter parameters are used for individual LV planes because the motion of the LV differs in SA planes. Similarly, the tagging pattern will deform independently in each plane. HPF has different filter parameters for each SA plane. After solving the harmonic images, the general optical flow equation [83] can be solved to obtain a deformation map entitled Harmonic Phase Flow [28]. Using the map, the motion of a single myocardial point can be quantified by analyzing its deformation throughout the cardiac cycle. The location of a single point at a time $t + 1$ is obtained by operating it with a motion vector that is calculated at time point t. The motion of the entire LV in a given plane is calculated by forming a continuous deformation map over the entire image series. Total rotation is solved as the least squares approximation to the rotations of all points inside the segmented myocardial wall. In HPF, torsion of the LV is calculated as the rotational difference between SA basal and apical planes of the LV, according to Equation 2.

HPF requires a single frame to be segmented by the user (Figure 5). The frame can be any frame between end-diastole and end-systole. In the end-diastolic frame, when any motion is yet to occur, only the clear grid pattern might be visible (Figure 6). In general, the delineation of the myocardial wall is easier and more reliable in early systole, when the heart begins rotating and tagged blood moves away from the imaging slice. Before rotation calculation, the frame where the reference boundaries have been drawn, the end-diastolic frame, and tagging grid orientation must be defined. HPF software then needs to extrapolate the segmentation to the last image of the tagging series and also to the first, the end-diastolic image. When the rotation of apical and basal planes has been calculated, torsion calculation is enabled. The software outputs scores of rotation and torsion from end-diastole (0%) to end-systole (100%).

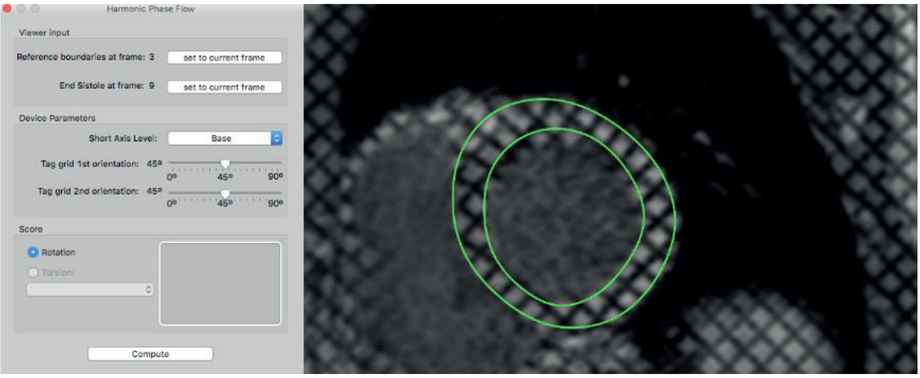

Reference boundaries at frame: 3

End Sistole at frame: 9

Short Axis Level: Base

Tag grid 1st orientation: 45°

Tag grid 2nd orientation: 45°

● Rotation

○ Torsion

Figure 5: Harmonic Phase Flow user interface and basal short-axis tagging image of the left ventricle with epicardial and endocardial segmentation. The frames of reference boundaries and end-systole, plane of analysis, and the tagging grid orientation have been manually defined for rotation analysis (Study IV).

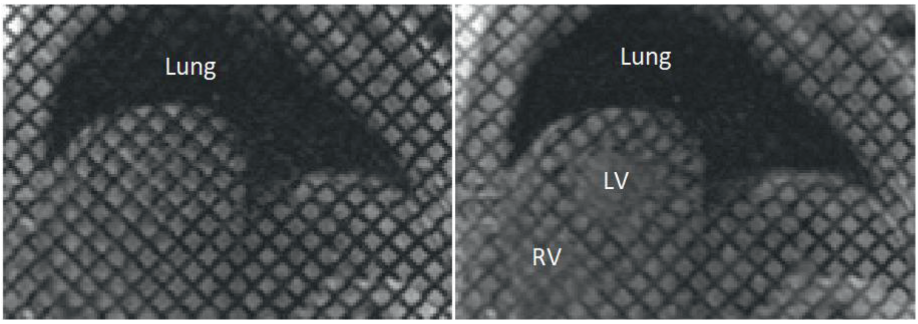

Figure 6: First (left) and third (right) tagging images of a mid-ventricular tagging image series. Left ventricle (LV) and right ventricle (RV) are not visible immediately after the tagging pattern creation, when motion is yet to occur.

The analysis of the tagging pattern can also be approached directly in the image space with non-rigid image registration-based methods. Initial methods focused on pairwise matching of tagging images [84], while more recently joint image matching has been proposed [85, 86]. The problem is that the comparison is commonly made only to the first image of the tagging series, which can be suboptimal due to tag fading. Morais et al. developed a sequential non-rigid registration method, which exploits temporal information based on image similarity. The method matches the entire tagging series instead of individual frames. This kind of method is implemented in the Segment strain module (Medviso AB, Lund, Sweden) [87, 88].

Non-rigid, or elastic registration methods use image warping to estimate deformation between image frames [89]. During image registration the image is deformed to match a reference image (typically first image of the series). The registration is an optimization problem where the goal is to find a displacement field $\mathbf{u}_{f\rightarrow f+1}(\mathbf{r})$ at each point $\mathbf{r}$ that makes image I_{f+1} spatially aligned with image I_f. Free-form deformation models parametrize the deformation field using smooth basis functions and have been an attractive approach to the problem. Segment software is based on this type of technique.

The sequential approach, with pairwise matching, describes the displacement $\mathbf{u}$ of a point $\mathbf{r} = [\mathrm{x}, \mathrm{y}]$ inside the segmented myocardium as a B-spline tensor product [90]:

$$\boldsymbol{u}_{f\rightarrow f+1}(\boldsymbol{r}) = \sum_{i\in N_x}\sum_{j\in N_y}\boldsymbol{\mu}^{ij}\,\beta_x^3\left(\frac{x-\kappa_x^i}{\sigma_x}\right)\beta_y^3\left(\frac{y-\kappa_y^j}{\sigma_y}\right), \tag{4}$$

where κ_ξ and σ_ξ are control point location and spacing, $\boldsymbol{\mu} = [\mu_x, \mu_y]$ are transformation field parameters, and N_ξ is a set of control points within the basis spline, or B-spline $\beta_\xi(\xi \in [x, y])$. Compared with thin-plate splines or elastic-body splines, B-splines are locally controlled, making them efficient computationally for a large group of control points [91]. The optimal frame-to-frame transformation field $\mathbf{T}(\mathbf{r}) = \mathbf{r} + \mathbf{u}_{f\rightarrow f+1}(\mathbf{r})$ can be estimated iteratively.

To utilize time in the transformation model, time needs to be included. This makes myocardial motion tracking a three-dimensional registration problem. The images I to be registered are two datasets represented by $F = \{I_i, i \in [1, N-1]\}$ and a temporally shifted version of F, denoted $M = \{I_j, j \in [2, N]\}$, with N frames in the tagging image sequence.

Direct inclusion of time leads to the transformation $\mathbf{T}(\mathbf{r}, t) = (\mathbf{r}, t) + \mathbf{u}_{F\rightarrow M}(\mathbf{r}, t)$, where the displacement field is as follows [88]:

$$\boldsymbol{u}_{F\rightarrow M}(\boldsymbol{r}, t) = \sum_{i\in N_x}\sum_{j\in N_y}\sum_{k\in N_t}\boldsymbol{\mu}^{ijk}\beta_x^3\left(\frac{x-\kappa_x^i}{\sigma_x}\right)\beta_y^3\left(\frac{y-\kappa_y^j}{\sigma_y}\right)\beta_t^3\left(\frac{t-\kappa_t^k}{\sigma_t}\right), \tag{5}$$

This approach has temporal information represented by a B-spline, which has compact support σ_t. The optimal field is obtained by optimizing the B-spline parameters, which is done by minimizing a cost function CF. The cost function determines what makes a set of coefficients either favorable or unfavorable.

When aligning the entire tagging image series, the cost function CF takes the form [88]:

$$CF = \frac{1}{d}\sum_{(r,t)\in F}\left[F(\boldsymbol{r},t) - M\left(\boldsymbol{T}(\boldsymbol{r},t)\right)\right]^2 + \frac{w_{BE}}{d}\sum_{(r,t)\in F}\left\|\frac{\partial^2 \boldsymbol{T}(r,t)}{\partial (r,t)^2}\right\|^2, \qquad (6)$$

where d is the number of points $\mathbf{r}$. The last term is the bending energy with w_{BE} a factor for its modulation, where $\mathbf{T} = [T_x, T_y, T_t]$ and $(\mathbf{r}, t)$ represent each point in the image sequence F.

Further modifications are required to prevent over-smoothing due to second-order derivatives in time. The transformation needs to be constrained to only cover registration between different frames. This can be done noting $\mathbf{u}_{F\to M} = [u_x, u_y, u_t]$ and setting $u_t = 0$, while keeping the spatial directions unchanged. This way, only in-plane gradients are used to update the transformation. Due to these restrictions in the optimizer, the terms $\frac{\partial^2 \mathbf{T}_t}{\partial\gamma\partial\gamma}(\mathbf{r}, t)$ will always remain zero since the gradient in this direction is never updated. Additionally, to prevent further penalties in the time direction, $\frac{\partial^2 \mathbf{T}_\xi}{\partial t\partial\gamma}(\mathbf{r}, t) = 0$, where $\gamma \in [x, y, t]$ and $\xi \in [x, y]$. With these modifications, the bending energy takes its final form [88]:

$$\left\|\frac{\partial^2 \boldsymbol{T}(r,t)}{\partial (r,t)^2}\right\|^2 = \sum_{\xi\in(x,y)}\left(\frac{\partial^2 \boldsymbol{T}_\xi}{\partial x^2}(\boldsymbol{r},t)\right)^2 + \left(\frac{\partial^2 \boldsymbol{T}_\xi}{\partial y^2}(\boldsymbol{r},t)\right)^2 + 2\left(\frac{\partial^2 \boldsymbol{T}_\xi}{\partial x\partial y}(\boldsymbol{r},t)\right)^2, \qquad (7)$$

This means that bending energy is the same form as a 2D formulation, and temporal smoothness is only applied by the temporal B-spline.

Strain of the myocardial wall is estimated based on user contouring. In each myocardial wall segment, the endocardial and epicardial contours consist of five and ten points in the radial and circumferential directions, respectively (Figure 7).

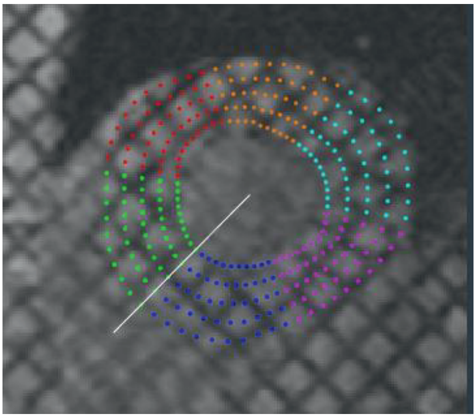

Figure 7: Short axis tagging view of the left ventricle with motion tracking points visible. Different colors note different segments of the AHA 17-segment model. The setting of the points is based on user-defined epicardial and endocardial contours.

It is noteworthy that the entire image content is used during the iteration process for optimal deformation field calculation and not just the segmented myocardial wall [92]. Like in HPF, the myocardial boundaries can be drawn in any of the frames between end-systole and end-diastole. User contour is then extrapolated to the entire tagging image series. The displacement of different analysis points is found by cumulating the transformation field [88]:

$$\boldsymbol{T}_{ED\to f}(\boldsymbol{r},t) = \boldsymbol{T}_{F\to M}(\boldsymbol{r},f-1) \circ \ldots \circ \boldsymbol{T}_{F\to M}(\boldsymbol{r},2) \circ \boldsymbol{T}_{F\to M}(\boldsymbol{r},ED)\,, \tag{8}$$

where ED denotes end-diastole, f an image frame, and $\mathbf{r} = [\mathrm{x}, \mathrm{y}]$. The calculation of strain in frame f then takes the familiar form of Equation 1:

$$\mathrm{strain}(f) = \frac{D_N(f) - D_N(ED)}{D_N(ED)} * 100\%. \tag{9}$$

$D_N(f)$ is the distance between two adjacent sample points in the direction N (circumferential, radial, or longitudinal) in frame f, $D_N(ED)$ being the matching distance at end-diastole. Segment reports strain results on the absolute time scale, not as a proportion of systole like HPF.

LV rotation can be calculated in SA slices. In different SA planes, the LV wall is approximately a circle. With SA images not acquired perfectly perpendicularly to the LA of the ventricle, the ventricular wall is more of an ellipsoid than a circle, introducing error to the axis of rotation calculation. Rotation is calculated based on the same deformation field (Equation 5) by fitting a circle to the LV segmentation [93]. The circle fitting in Segment is done by minimizing the global squared radial difference in all time frames between the tracking points $(x_i, y_i), i = 1 \ldots N$ of the segmentation and a circle with a radius $r = \sqrt{a}$. After the axis of rotation has been fitted to each temporal image frame with segmentation points, the points are translated so that each center of axis of rotation is in origo. This is because angular discontinuity needs to be detected prior to rotation calculation. A change from a Cartesian coordinate system to a polar one results in a line-like formation of the segmentation points. The movement of this line along the θ axis is myocardial rotation in the plane of analysis. In Segment, torsion is defined as the rotational difference between apical and basal slices, normalized with the longitudinal distance between the two slices and the mean radius of segmented ventricular wall, the unit of torsion being °/mm.

3.4.2 FEATURE TRACKING

FT is quantitative post-processing for motion extraction of cine images [94]. Technologically, the underlying principle is based on recognizing patterns in cine images, and following them throughout the cardiac cycle [95]. FT algorithms, require optimization with adjustments for sufficient image quality, temporal resolution of the image series, and magnitude and speed of the displacements expected [8].

Segment software uses the same non-rigid registration algorithm for strain analysis with FT of conventional cine images. The spline-based tracking in image space is independent of the tagging pattern. FT is dependent on contrast differences; motion tracking cannot be performed on homogeneous targets such as intramyocardial tissue. Thus, rotation and torsion analysis are only recommended with tagging images. Cine images selected for FT analysis require consistent methodology for slice selection. Cine images are commonly acquired throughout the heart, and the selection of basal, mid-ventricular, and apical planes needs to be consistent for reliable and repeatable analysis between different subjects. Optimal basal slice is the slice closest to the annulus of the LV, without throughplane distortion from the LV outflow tract. Mid-ventricular slice is the slice that is equidistant from the LV apex and the mitral valve plane, while apical slice is equidistant between the apical cap of the LV and the mid-ventricular plane.

4 AIMS OF THE STUDY

This thesis aimed to assess myocardial tagging and feature tracking in the analysis of quantitative myocardial motion. The studies were designed to:

1) investigate whether quantitative global, planar, and segmental myocardial motion parameters would bring additional value over conventional volumetric measurements in:
- rheumatoid arthritis (RA, Study I)
- tetralogy of Fallot (TOF, Study II)
- hereditary gelsolin amyloidosis (Study III)
- hypertrophic cardiomyopathy (HCM, Study IV).

2) evaluate quantitative global, planar, and segmental motion against quantitative tissue measures (late gadolinium enhancement, T1, or extracellular volume) (Studies I and III) and volumetric measurements (Study II).

3) evaluate intra-observer variability (Studies II and IV), examine performance of different technical approaches in rotation and torsion analysis (Study IV), and create datasets of different motion parameters that can be used as references for healthy and diseased myocardium (Studies I-III).

5 MATERIALS AND METHODS

5.1 STUDY DESIGN AND PROTOCOL

The studies in this thesis developed from analyzing the motion of LV, evolving to analyze both LV and RV. The study populations and analyzed parameters in the sub-studies are combined in Table 1.

Table 1: Analyzed parameters in Studies I-IV.

Study	Study population	Motion parameters	Other analysis
I	Rheumatoid arthritis	LV strain (tagging)	T1, LGE
II	Tetralogy of Fallot & healthy controls	LV & RV strain (FT)	Pulmonary regurgitation, intra-observer variability
III	Hereditary gelsolin amyloidosis	LV & RV strain (FT), LV rotation & torsion (tagging)	T1, ECV, LGE
IV	Hypertrophic cardiomyopathy & healthy controls	LV rotation & torsion (tagging)	Intra-observer-variability

LV = left ventricle, LGE = late gadolinium enhancement, RV = right ventricle, FT = feature tracking, ECV = extracellular volume

Studies I, II, and IV were retrospective analyses of previously acquired CMR data, while Study III was prospective. All studies received ethical approval from the Ethics Review Board of Helsinki and Uusimaa, and a written informed consent was obtained from each participant.

Study I was a follow-up study of patients with active RA. The study comprised 39 patients with active RA who were selected from a previous study population of 60 patients with active RA. To minimize the risks of patients having disorders other than RA that could affect the myocardium, the study population of 60 individuals included only non-smoking, non-diabetic females under the age of 70 years who had no severe obesity. All 60 patients had two CMR examinations (total of 120); of these patients 21 had severe cardiac gating or breathing-induced image artifacts at either baseline or one year after the baseline. The 39 patients selected for this study had successfully undergone CMR studies at baseline and one year after baseline, with sufficient image quality for quantitative analysis of tagging and native T1 mapping sequences. RA disease activity score (DAS28-CRP) was also assessed before and after the one-year treatment period. The study population was split into early RA (duration of symptoms 11 ± 15 months, no previous treatment, N = 25) and chronic RA (duration of symptoms 207 ± 133 months, inadequate response to conventional treatment, N = 14). Subjects with early RA were treated with conventional synthetic disease-modifying antirheumatic drugs, and chronic subjects received biological drugs. Study subjects had undergone a CMR study using either a 1.5T (N = 16) or 3T (N = 23) MR system (Avanto^{fit} and Verio, Siemens Healthcare, Germany) and a 32-channel cardiac coil. Each study subject was imaged using the same MR system at baseline and at the one-year follow-up. The CMR protocol included bSSFP cine images of the LV in SA and 4CH LA direction. SPAMM tagging, shortened modified look-locker inversion recovery T1 mapping, and inversion recovery spoiled gradient-echo late gadolinium enhancement (LGE) images were all acquired at mid-ventricular SA plane of the LV. Additionally, tagging images were acquired in the LA 4CH direction. Cine and tagging images all had 25 temporal phases. Mid-ventricular SA and 4CH LA tagging images were analyzed for segmental peak systolic strain, peak systolic strain rate, and peak diastolic strain rate. Strain values were collected in all six segments of the mid-ventricular LV in the SA direction, and as mean in the LA direction. Changes in strain during the follow-up were compared with RA disease activity score and late gadolinium enhancement (LGE).

Study II included 45 adolescent patients who had had surgical repair of TOF between 1990 and 2003. The patients were referred to CMR by a pediatric cardiologist, based on echocardiographic findings that suggested significant pulmonary regurgitation (PR) and increased RV size. Three patients declined to participate in the CMR study and two were rejected due to insufficient CMR image quality. Thus, 40 patients (mean age 13±3 years, 38% females) were included in the final study. Forty-four healthy adolescents with similar age and gender distribution (mean age 14±3 years, 39% females) were recruited as control subjects. The admission criteria of healthy controls were 1) no medical history of cardiovascular diseases and 2) no other known conditions that would affect the cardiovascular system. Morphological echocardiography and ECG recording were performed to exclude possible latent cardiac problems. CMR examination was performed on all subjects and controls using a 1.5T Achieva MR system (Philips Healthcare, The Netherlands) with a 5-channel cardiac coil. Transaxial and SA cine images were acquired throughout the heart. Cine images had 30 and 25 temporal phases in the SA and LA directions, respectively. The cine images of adolescents with repaired TOF (N = 40) and healthy controls (N = 44) were retrospectively analyzed for peak LV and RV systolic strain, peak systolic strain rate, and peak diastolic strain rate using FT. Additionally, strain curves were compared visually by calculating mean strain curves of the study groups. Results were collected in SA planes and in 4CH LA direction for both ventricles. Results were compared separately between TOF patients and healthy controls and between TOF patients with mild (N = 29) and severe (N = 11) pulmonary regurgitation (PR).

In Study III, 50 patients with Finnish hereditary gelsolin amyloidosis were included from the patient registry of Finnish Gelsolin amyloidosis (FIN-GAR). Exclusion criteria of the study were as follows: 1) age below 50 years, 2) implanted cardiac pacemaker, 3) claustrophobia, and 4) implanted metal objects that could interfere with the CMR examination. Age below 50 years was an exclusion criterion due to disease progression beginning at an older age [28, 79, 80]. All subjects (mean age 66±7 years) were prospectively imaged with a 1.5T Avanto$^{\mathrm{fit}}$ MR scanner (Siemens Healthcare, Germany) using a 32-channel cardiac receiver coil with retrospective ECG-gating. Images were acquired in breath-hold to minimize breathing-related artifacts. The CMR protocol included bSSFP cine images with 30 temporal phases in SA and LA 4CH directions, SPAMM tagging, pre-contrast and post-contrast shortened modified look-locker inversion recovery T1 mapping, and inversion recovery spoiled gradient-echo LGE images. T1 mapping, tagging, and LGE sequences were all acquired in the same basal, mid-ventricular, and apical planes according to the AHA segment model. All study subjects had their hematocrit measured via blood test after the CMR study. LV rotation and torsion were analyzed with tagging images, and mean peak strain, peak systolic strain rate and peak diastolic strain rate were analyzed for both LV and RV. LV strain parameters, T1, extracellular volume, and late gadolinium enhancement values were compared in 16 segments of the AHA segment model.

In Study IV, the study population was selected from a previous study of myosin-binding protein C gene (MYBPC). The population consisted of 32 patients carrying the Finnish founder mutation in the MYBPC gene (MYBPC3-Q1051X) with LV hypertrophy consistent with HCM phenotype (LV maximal wall thickness > 13 mm), 15 subjects with the mutation but no HCM phenotype (LV maximal wall thickness < 13 mm), and their 20 healthy relatives with no mutation [96]. Genetic diagnosis was confirmed on all subjects [97]. Of these individuals, 36 (14 HCM patients, age 43±11 years; 10 mutation carriers, age 34±13 years; and 12 healthy relatives, age 43±17 years) had undergone CMR studies using a 1.5T Avanto$^{\mathrm{fit}}$ MR (Siemens Healthcare, Germany) with successful tagging images acquired and were selected for the study. In the CMR study, SPAMM tagging images were acquired in apical and basal SA levels of the LV. In this study, the feasibility of a non-rigid elastic image registration scheme (Segment) and a HARP-based method with Gabor filtering (HPF) was compared in the analysis of myocardial tagging for systolic rotation and torsion in SA direction of the LV. Basal and apical SA tagging images were retrospectively analyzed with both software packages.

5.2 ANALYZED PARAMETERS

This thesis employed two software solutions for the analysis of quantitative myocardial motion: the Segment strain module (Medviso AB, Lund, Sweden) [87, 88], which was used to analyze rotation and torsion (Studies III and IV), strain in tagging images (Study I), and strain in conventional cine images (Studies II and III); and Harmonic Phase Flow (HPF) plugin (Computer Vision Center, Barcelona, Spain) [28, 79, 80], which was used to analyze systolic rotation and torsion in tagging images (study IV). In the studies, cine image slice selection for FT analysis was done at end-diastole according to the recommendations by Taylor et al. [98]. Motion quantification from CMR tagging and cine images required segmentation of the cardiac muscle wall. With both software used here, a single time frame was manually contoured in the given ventricle and cardiac plane of analysis, prior to all motion analyses. The rest of the image sequences were segmented automatically based on user contouring. Tracking quality of both tagging (Studies I, III, and IV) and cine images selected for FT analysis (Studies II and III) was assessed by visually reviewing the tracked contour throughout the cardiac cycle. If inaccurate tracking was detected, the contouring was manually corrected before advancing to motion analysis. When the tracking was deemed reliable, the resulting strain curves were visually compared with the tracked contour. The visual evaluation was done in each cardiac plane, and when segmental results were collected, individually for each segment. Particular attention was paid to verifying that the strain curves returned to baseline level.

Segmental LV SA strain curves derived with tagging (Study I; circumferential direction) and cine images (Studies II and III; circumferential and radial directions) were imported to MATLAB (The MathWorks Inc., Natick, MA, USA) to calculate peak systolic strain and peak strain rate (systolic and diastolic). Peak SA planar strain values (Study I: LV mid-ventricular; Studies II and III: basal, mid-ventricular, and apical) were calculated as segmental means. Mean LV SA strain (circumferential and radial) was calculated as a mean of planar values.

Peak longitudinal strain parameters (Studies I- III) were calculated as a mean (no segmental division) of the entire ventricular walls in LA 4CH tagging or cine images. Similarly, peak RV SA planar and RV longitudinal strain parameters (Studies II and III) were calculated as a mean of the entire RV wall in SA and LA 4CH cine images. Figure 8 displays examples of LV and RV SA mid-ventricle and LV and RV LA 4CH cine images with manual contours.

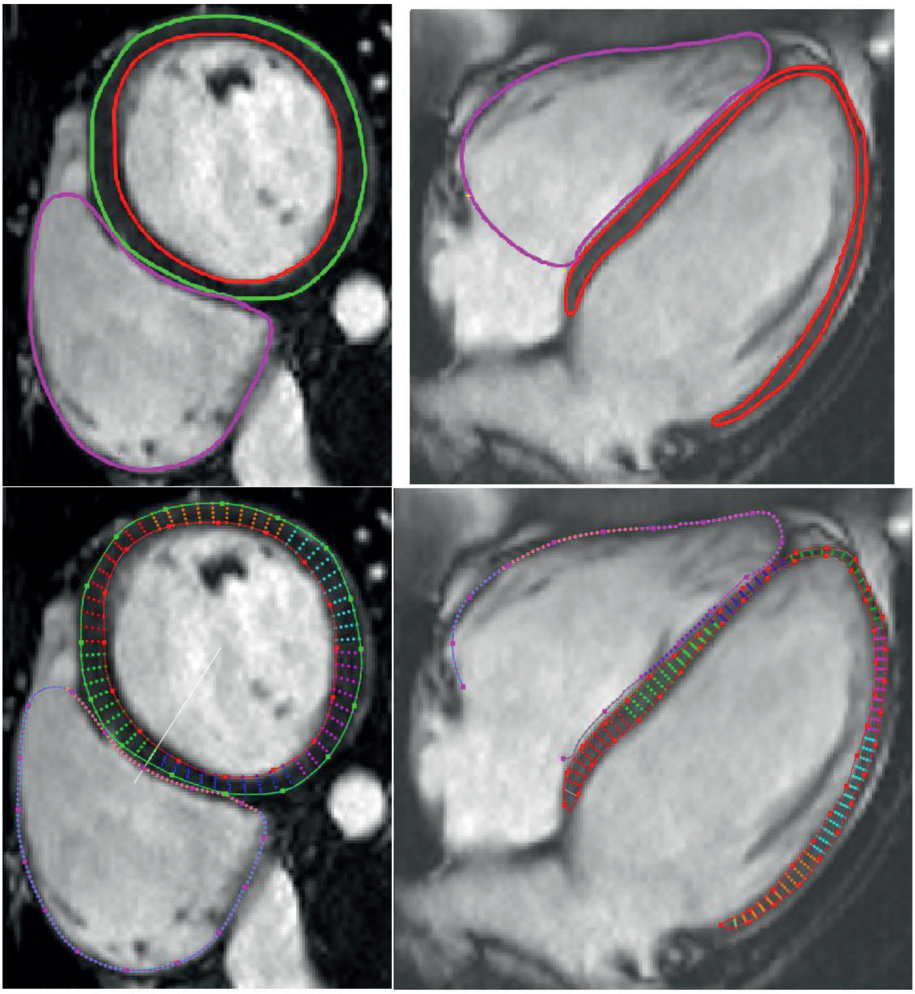

Figure 8: Upper row: end-diastolic basal short-axis (left) and long-axis four-chamber (right) cine images with manual segmentation of the left ventricle and right ventricle. The left ventricle has both endocardial and epicardial segmentation, while the right ventricle only has endocardial segmentation. Bottom row: end-diastolic view of motion tracking points for left ventricle and right ventricle in basal short-axis (left) and long-axis four-chamber (right) direction. Different colors of the tracking points denote different segments of the ventricles. After manual segmentation of the ventricles, manual correction of the tracking points is possible in any frame of the cardiac cycle.

Study II was, additionally to peak strain analysis, motivated by visual comparison of strain curves between study groups. To obtain mean strain curves of different study populations for visual comparison, average values for each temporal phase and strain value were calculated. For example, the time point of the 10th temporal phase in the mean curve was calculated as the average of the 10th temporal phase of all individuals comprising the mean curve. A similar approach was used to obtain each strain value in the mean curve. Examples of LV and RV longitudinal strain curves of 11 subjects and their calculated mean curves are presented in Figure 9. The method was further extended to convert strain curves to match a specific RR interval. When the number of sampling points, or temporal phases, is the same in the strain curves, a specific RR interval fixes the time point of each temporal phase. This approach was used to match the mean strain curves for visual comparison in Study II. It should be noted that this kind of visualization does not represent the true strain behavior of any individual.

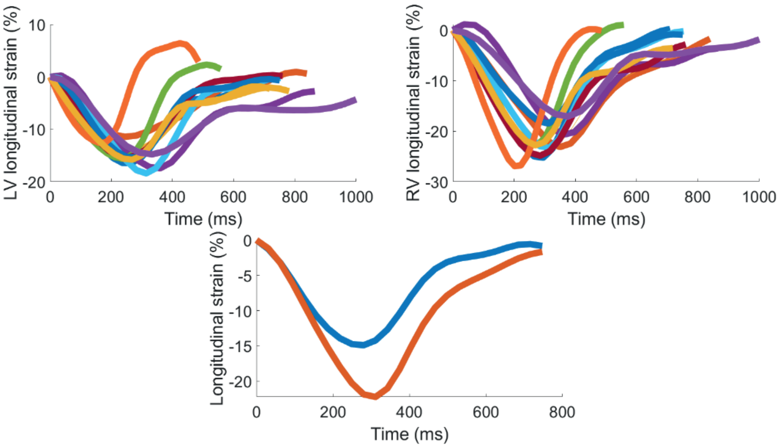

Figure 9: Top: longitudinal strain curves of left ventricle (LV) and right ventricle (RV) in different individuals (N = 11) with different length RR intervals. Bottom: calculated mean of the above curves (blue = LV, orange = RV).

Volumetric parameters were measured in all studies from cine images. Parameters included indexed end-systolic and end-diastolic volumes of the LV and EF. Analyses were performed with QMass MR software v7.6 (Medis Medical Imaging Systems, Leiden, The Netherlands; Studies I, III, IV) and with Philips ViewForum workstation (Philips Healthcare, The Netherlands; Study II). PR [ml/m^2] (Study II) was evaluated based on ventricular volumetric measurements. All volumetric analyses were performed by experienced radiologists and cardiologists.

T1 mapping images were analyzed in all six segments of mid-ventricular SA plane with QMass MR software v7.6 (Medis Medical Imaging Systems, Leiden, The Netherlands) (pre-contrast, Study I) with manual contouring. In Study III, the analysis was performed according to the AHA segment model with Segment (Medviso AB, Lund, Sweden) (pre-contrast and post-contrast). Regions of interest (ROIs) according to the AHA segment model were placed automatically based on segmentation of FT images of the LV. The analysis ROIs were cropped 20% from the epicardium and endocardium to avoid signal inhomogeneities. The ROIs of the pre-contrast images were copied to the post-contrast images, and matching of AHA segments in pre-contrast images and post-contrast images was visually verified. Based on pre-contrast and post-contrast T1 relaxation times, extracellular volume (ECV) was evaluated using the following equation [99]:

$$ECV = (1 - hematocrit)\left(\frac{\frac{1}{post\ contrast\ T1\ myocardium} - \frac{1}{pre\ contrast\ T1\ myocadium}}{\frac{1}{post\ contrast\ T1\ blood} - \frac{1}{pre\ contrast\ T1\ blood}}\right) \qquad (10)$$

LGE images were analyzed according to the AHA segment model by experienced radiologists visually (Studies I and III) and computationally with Qmass MR software (Medis Medical Imaging Systems, Leiden, The Netherlands) using a full width at half-maximum method with a 50% threshold (Study III). Visual analysis divided LV segments into those with and those without LGE. Computational analysis resulted in LV LGE percentage.

Statistical analysis of the results in different studies was performed with MATLAB R2016A (The MathWorks Inc., Natick, MA, USA) (Study I) and IBM SPSS Statistics for Windows, versions 24 and 25 (IBM Corp., Armonk, NY, USA) (Studies II-IV). Results of continuous parameters are reported as mean ± standard deviation or as median (Q1-Q3). Differences were analyzed using the Wilcoxon signed-rank test (Study I), independent samples Student's t-test (Studies II and III), and independent samples Kruskal-Wallis test (Study IV). Pearson correlation (Studies I-III) and Spearman's rho (Study IV) were used to test for correlations between different parameters. Error of the visual mean strain representations (Study II) was evaluated using standard deviation of the study samples. Intra-observer variability (N = 30) of LV and RV strain was assessed using intraclass correlation coefficient (ICC) and the Bland-Altman method (Study II), and intra-observer variability of rotation and torsion (N = 36) with the Bland-Altman method (Study IV).

6 RESULTS

6.1 EARLY AND CHRONIC RHEUMATOID ARTHRITIS

During the one-year follow-up the peak circumferential diastolic strain rate improved for patients with early RA (before treatment: 82 [74–91] %/s vs. after treatment: 91 [77–100] %/s, p = 0.05). The improved strain rate of early RA was most significant in the anterior segment of the mid-level of the LV (before treatment: 82 [63–98] %/s vs. after treatment: 85 [77–109] %/s, p = 0.013) (Table 2). Changes in the RA disease activity score (DAS28-CRP) correlated with the improvement of peak mean circumferential diastolic strain rate in patients with early RA (Figure 10). Similar observations were not made for patients with chronic RA (data not presented). Peak systolic SA (circumferential) or LA strain values did not change significantly in either study group. Changes in T1 relaxation times or LGE were not associated with different strain parameters in either study group.

Table 2: Results of strain tagging analysis for early RA patients (n = 25) (Study I).

Segment	Before treatment	After treatment	Change	p-value
	Peak systolic SA strain (%)			
Anterior	-21.6 (-24.2 - (-19.8))	-22.0 (-24.8 - (-19.4))	0.1 (-2.1 - 1.6)	0.76
Anteroseptal	-17.0 (-19.8 - (-15.4))	-17.6 (-21.1 - (-16.5))	-0.2 (-2.6 - 1.2)	0.76
Inferoseptal	-15.0 (-17.6 - (-12.2))	-16.2 (-18.5 - (-14.4))	-1.1 (-2.7 - 1.2)	0.08
Inferior	-18.7 (-19.9 - (-16.4))	-17.5 (-22.6 - (-15.4))	0.4 (-2.2 - 2.2)	0.89
Inferolateral	-20.8 (-23.9 - (-18.7))	-21.6 (-23.6 - (-15.4))	-0.7 (-2.8 - 1.0)	0.39
Anterolateral	-19.8 (-20.8 - (-17.3))	-20.5 (-21.9 - (-17.1))	0.7 (-0.7 - 2.1)	0.93
All segments	-18.9 (-20.8 - (-16.6))	-19.3 (-21.3 - (-17.0))	-0.4 (-1.6 - 0.8)	0.20
	Peak diastolic SA strain rate (%/s)			
Anterior	82.2 (63.3 - 98.4)	85.5 (76.5 - 109.2)	18.7 (3.1 - 26.4)	0.01*
Anteroseptal	82.0 (75.8 - 97.0)	95.8 (78.1 - 102.7)	5.5 (-6.7 - 22.7)	0.16
Inferoseptal	71.0 (64.7 - 81.3)	79.0 (64.6 - 92.8)	2.2 (-7.8 - 11.5)	0.39
Inferior	77.2 (65.9 - 97.4)	84.7 (67.6 - 92.8)	2.6 (-13.0 - 21.4)	0.43
Inferolateral	89.3 (83.8 - 120.8)	103.4 (75.6 - 133.6)	8.0 (-21.9 - 33.3)	0.66
Anterolateral	76.6 (61.3 - 90.6)	88.7 (73.1 - 105.6)	14.6 (-10.1 - 36.4)	0.09
All segments	82.3 (73.9 - 90.7)	91.1 (77.0 - 100.1)	7.7 (-8.2 - 23.4)	0.05*
	Peak systolic LA strain (%)			
Mean	-15.0 (-16.4 - (-13.1))	-14.1 (-15.6 - (-12.6))	0.5 (-0.8 - 1.6)	0.55
	Peak diastolic LA strain rate (%/s)			
Mean	42.0 (32.7 - 49.1)	43.2 (34.9 - 49.7)	-0.1 (-9.1 - 9.9)	0.67

Results are expressed as median (Q1 - Q3), SA = short axis, LA = long axis, *statistically significant change.

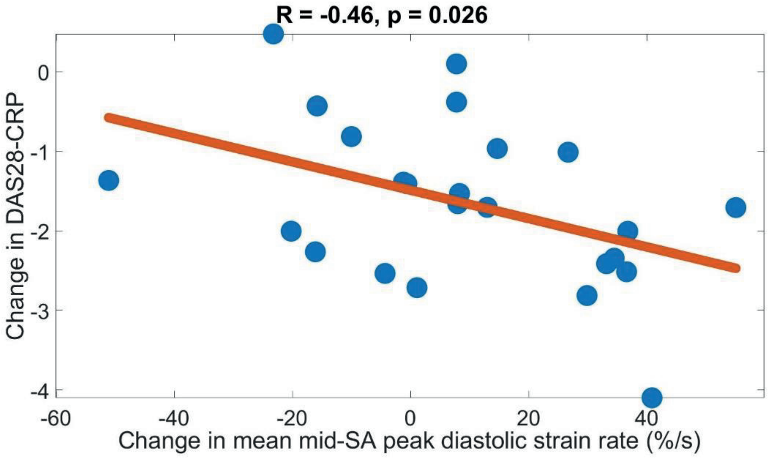

Figure 10: Correlation with the change in DAS28-CRP disease activity score and mean mid-*SA* diastolic strain rate in early rheumatoid arthritis (n = 25), SA = short axis (*S*tudy I).

6.2 TETRALOGY OF FALLOT

RV peak longitudinal strain was increased in TOF patients with severe PR (>30 ml/m^2) compared with TOF patients with mild PR (<30 ml/m^2) (−23% ± 3% vs. −20% ± 4%, p = 0.01) and healthy controls (−23% ± 3% vs. -19% ± 3%, p = 0.007). TOF patients with mild PR had no significant difference in RV longitudinal strain compared with healthy controls. LV peak strain, systolic strain rate, or diastolic strain did not differ significantly between TOF patients and healthy controls or between TOF patients with severe and mild PR.

Looking at other strain parameters, significant differences between study groups were detected in RV circumferential strain (Table 3). These differences were also seen in the strain curves of different study groups (Figure 11). Mean RV circumferential strain differed significantly between TOF patients and healthy controls, but did not differ significantly between the TOF subgroups. In different SA planes of the RV, peak circumferential strain gradually increased from base to apex in patients with TOF (Table 4, Figure 12). The increase was highest in the mid-ventricular and apical levels of the RV. A similar finding was made in healthy controls, however, the increase was higher in patients with TOF (apex-base difference 8% ± 4% vs. 3% ± 2%, p < 0.0001), in whom peak RV circumferential strains were significantly different in basal, mid-ventricular, and apical planes. PR did not explain the increase of RV circumferential strain in TOF patients.

Table 3: Results for right ventricle strain parameters in healthy controls and in patients with TOF having pulmonary regurgitation (Study II).

Parameter	Healthy	TOF	p-value	TOF (PR < 30ml/m^2)	TOF (PR > 30ml/m^2)	p-value
RV circumferential	N=44	N=40		N=29	N=11	
Strain (%)	-12 ± 3	-17 ± 4	< 0.0001*	-17 ± 4	-17 ± 4	0.69
Systolic strain rate (%/s)	-60 ± 21	-80 ± 23	< 0.0001*	-78 ± 20	-85 ± 32	0.47
Diastolic strain rate (%/s)	61 ± 19	87 ± 33	< 0.0001*	84 ± 32	94 ± 36	0.45
RV longitudinal	N=40	N=35		N=24	N=11	
Strain (%)	-19 ± 3	-21 ± 4	0.15	-20 ± 4	-23 ± 3	0.02*
Systolic strain rate (%/s)	-84 ± 19	-99 ± 23	0.002*	-95 ± 20	-110 ± 27	0.12
Diastolic strain rate (%/s)	81 ± 27	107 ± 33	0.0001*	102 ± 27	124 ± 40	0.10

PR = pulmonary regurgitation, RV = right ventricle, TOF = repaired tetralogy of Fallot, *statistically significant difference ($p < 0.05$)

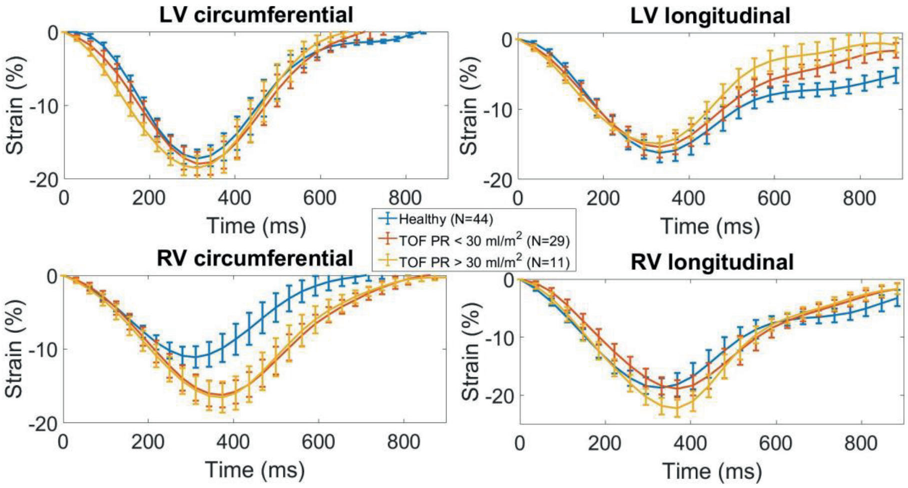

Figure 11: Mean strain curves of analyzed strain parameters in patients with repaired tetralogy of Fallot (TOF) (PR < 30 ml/m^2 or PR > 30 ml/m^2) and healthy controls. Heart rate has been fixed to 68 beats per minute (average heart rate of healthy controls). Error bars were evaluated as standard deviation of the samples. LV = left ventricle, RV = right ventricle, PR = pulmonary regurgitation (Study II).

Table 4: Peak circumferential strain in three planes of the right ventricle of healthy controls and of patients with TOF having pulmonary regurgitation (study II).

RV plane	Healthy (N=44)	TOF (N=40)	p-value	TOF PR < 30 30ml/m^2 (N=29)	TOF PR > 30 30ml/m^2 (N=11)	p-value
Base	-11 ± 3	-13 ± 4	0.01*	-13 ± 4	-14 ± 3	0.34
Mid	-11 ± 3	-17 ± 4	< 0.0001*	-17 ± 4	-17 ± 5	0.64
Apex	-14 ± 4	-20 ± 5	< 0.0001*	-21 ± 5	-20 ± 6	0.88

RV = right ventricle, TOF = repaired tetralogy of Fallot, PR= pulmonary regurgitation ml/m^2, *statistically significant difference ($p < 0.05$)

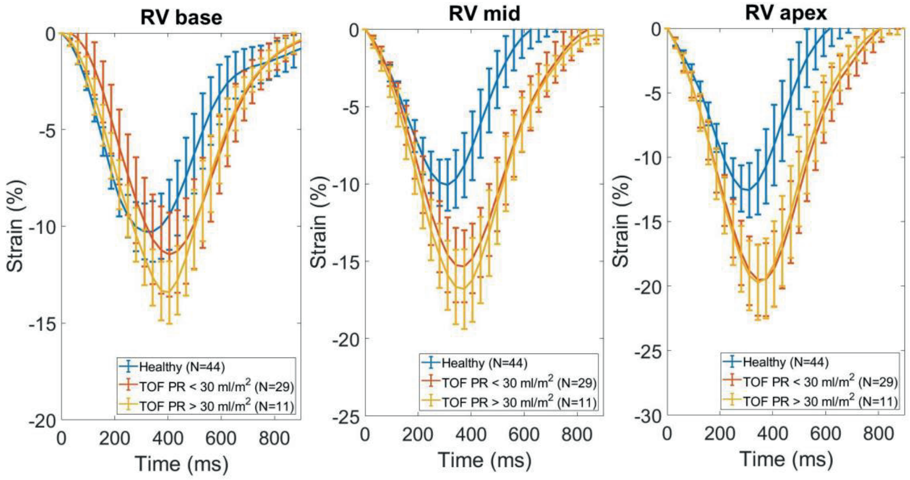

Figure 12: Mean strain curves of right ventricular circumferential strain in different short-axis planes. Heart rate has been fixed to 68 beats per minute (average heart rate of healthy controls). Error bars were evaluated as standard deviation of the samples. (Study II).

6.3 HEREDITARY GELSOLIN AMYLOIDOSIS

Segmental strain and strain rate values of different LV segments are displayed in Table 5. At basal level of the LV, peak circumferential strain values of inferoseptal and inferior segments were significantly lower ($p < 0.001$) than those of other segments of the basal plane. Similarly, peak radial strain in the same basal region was reduced ($p < 0.005$). In the mid-ventricular LV plane, inferior and anterolateral segments had decreased peak circumferential strain and peak diastolic circumferential strain rate. Radial strain parameters had no significant differences between segments. In the apical plane, no significant differences in any of the strain values between segments were detected.

Mean circumferential strain values of different planes were similar in basal and mid-ventricular planes, and were highest in the apical plane, in both ventricles. Longitudinal strain values were higher in RV than in LV ($p < 0.007$).

Table 5: Results for segmental and mean strain and strain rate analysis of both ventricles in hereditary gelsolin amyloidosis (n = 50) (Study III).

Short-axis	**Peak CS (%)**	**Peak systolic CSR (%/s)**	**Peak diastolic CSR (%/s)**	**Peak RS (%)**	**Peak systolic RSR (%/s)**	**Peak diastolic RSR (%/s)**
LV mean	-20 ± 3	-94 ± 17	87 ± 22	55 ± 10	233 ± 44	-274 ± 59
LV base	-18 ± 3	-80 ± 14	74 ± 16	51 ± 13	206 ± 56	-235 ± 70
LV mid	-18 ± 3	-83 ± 21	79 ± 21	58 ± 12	254 ± 56	-301 ± 85
LV apex	-24 ± 6	-120 ± 31	106 ± 41	55 ± 15	239 ± 63	-284 ± 82
RV mean	-14 ± 4	-70 ± 20	64 ± 20	NA	NA	NA
RV base	-12 ± 4	-61 ± 21	47 ± 14	NA	NA	NA
RV mid	-15 ± 5	-69 ± 23	65 ± 29	NA	NA	NA
RV apex	-15 ± 7	-78 ± 31	79 ± 35	NA	NA	NA
Long-axis	**Peak LS (%)**	**Peak systolic LSR (%/s)**	**Peak diastolic LSR (%/s)**			
LV mean	-17 ± 3	-79 ± 15	61 ± 14			
RV mean	-22 ± 4	-96 ± 19	67 ± 19			
LV segments	**Peak CS (%)**	**Peak systolic CSR (%/s)**	**Peak diastolic CSR (%/s)**	**Peak RS (%)**	**Peak systolic RSR (%/s)**	**Peak diastolic RSR (%/s)**
Basal anterior	-21 ± 6	-112 ± 32	98 ± 34	56 ± 19	246 ± 79	-279 ± 109
Basal anteroseptal	-19 ± 6	-90 ± 27	70 ± 27	**34 ± 15***	**169 ± 68***	**-175 ± 79***
Basal inferoseptal	**-14 ± 5***	-73 ± 21	81 ± 23	**27 ± 9***	**134 ± 46***	**-160 ± 51***
Basal inferior	**-16 ± 6***	-76 ± 25	78 ± 25	62 ± 19	276 ± 96	-350 ± 127
Basal inferolateral	-21 ± 7	-97 ± 31	128 ± 40	71 ± 16	315 ± 96	-361 ± 124
Basal anterolateral	-22 ± 7	-99 ± 30	112 ± 40	70 ± 19	308 ± 93	-361 ± 129
Mid anterior	-21 ± 6	-110 ± 23	97 ± 30	65 ± 14	291 ± 64	-383 ± 111
Mid anteroseptal	-20 ± 6	-115 ± 26	102 ± 30	52 ± 15	272 ± 74	-277 ± 78
Mid inferoseptal	-21 ± 7	-108 ± 31	114 ± 34	55 ± 16	276 ± 80	-271 ± 95
Mid inferior	**-15 ± 5***	**-72 ± 23***	87 ± 40	59 ± 14	264 ± 70	-309 ± 94
Mid inferolateral	-20 ± 5	-92 ± 28	119 ± 46	62 ± 14	274 ± 77	-371± 139
Mid anterolateral	**-15 ± 5***	**-75 ± 27***	**68 ± 33***	62 ± 15	270 ± 74	-399 ± 151
Apical anterior	-23 ± 6	-122 ± 33	111 ± 40	59 ± 20	263 ± 86	-331 ± 122
Apical septal	-27 ± 7	-144 ± 38	130 ± 51	45 ± 16	207 ± 69	-249 ± 80
Apical inferior	-26 ± 8	-127 ± 40	131 ± 50	56 ± 13	259 ± 63	-291 ± 72
Apical lateral	-20 ± 6	-111 ± 40	98 ± 43	65 ± 19	295 ± 82	-371 ± 127

CS = circumferential strain, CSR = circumferential strain rate, RS = radial strain, RSR = radial strain rate, LV = left ventricle, RV = right ventricle, NA = not applicable, LS = longitudinal strain, LSR = longitudinal strain rate, *significantly reduced ($p < 0.05$) from other (half or more) segments of the same plane.

6.4 HYPERTROPHIC CARDIOMYOPATHY

In Study IV, analysis time of rotation and torsion was 4 ± 2 minutes with HPF (harmonic phase) and 5 ± 2 minutes with Segment (non-rigid registration). End-systolic peak apical rotation and peak basal rotation and torsion are reported in Table 6. Results did not differ significantly between the study groups with either software. HPF showed constantly smaller peak values than Segment ($p < 0.0001$). Observations were similar in all study groups. Peak apical rotation was highest in mutation carriers with both software, together with peak torsion. Systolic rotation and torsion curves of both software showed visually similar paths.

Table 6: End-systolic rotation and torsion values in different study groups analyzed with HPF and Segment (Study IV).

Parameter	**HCM** N = 14	**Mutation** N = 10	**Healthy** N = 12	**p-value**
HPF apical rotation (°)	1.8 ± 1.8	3.0 ± 1.7	1.9 ± 1.9	0.27
HPF basal rotation (°)	-1.5 ± 1.2	-1.1 ± 0.9	-1.9 ± 1.3	0.35
HPF torsion (°)	3.3 ± 1.7	4.1 ± 1.6	3.8 ± 1.3	0.36
Segment apical rotation (°)	3.4 ± 4.5	6.0 ± 2.3	4.0 ± 4.3	0.46
Segment basal rotation (°)	-3.8 ± 2.5	-3.6 ± 2.3	-4.0 ± 2.5	0.67
Segment torsion (°)	7.2 ± 3.7	9.5 ± 2.2	8.0 ± 2.6	0.15
Segment torsion, normalized (°/mm)	0.2 ± 0.1	0.2 ± 0.1	0.2 ± 0.1	0.20

HCM = hypertrophic cardiomyopathy, HPF = Harmonic Phase Flow

The rotation and torsion values obtained with the two software packages correlated significantly (Figure 13). Apical plane rotation showed the highest correlation between the two software (ρ > 0.9), while basal rotation did not agree as strongly (ρ > 0.6). As torsion is the rotational difference between apical and basal planes, its correlation between the software was stronger than that for basal rotation (ρ > 0.7).

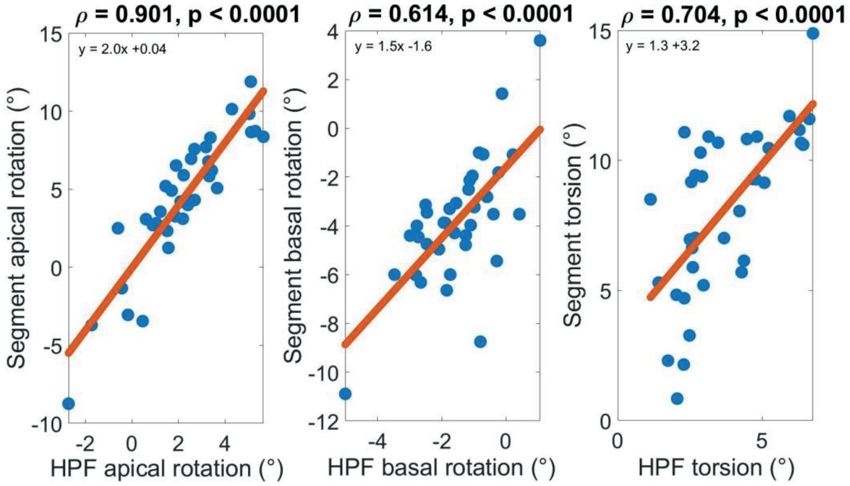

Figure 13: Correlations between end-systolic rotation and torsion values obtained with Segment and Harmonic Phase Flow (HPF) (Study IV).

6.5 CORRELATION OF MYOCARDIAL MOTION WITH OTHER MRI-DERIVED PARAMETERS

In Study I, significant correlations ($p < 0.001$) were detected between the changes in peak LV systolic strain and peak diastolic strain rate in SA and LA directions in the entire study population of 39 subjects with RA, whether the changes were positive or negative (Figure 14).

In Study II, PR volume and RV longitudinal strain parameters correlated significantly ($p \leq 0.03$) in TOF patients (Figure 15). Patients with increased PR had on average higher RV peak longitudinal strain and peak systolic and diastolic strain rate in the TOF study group.

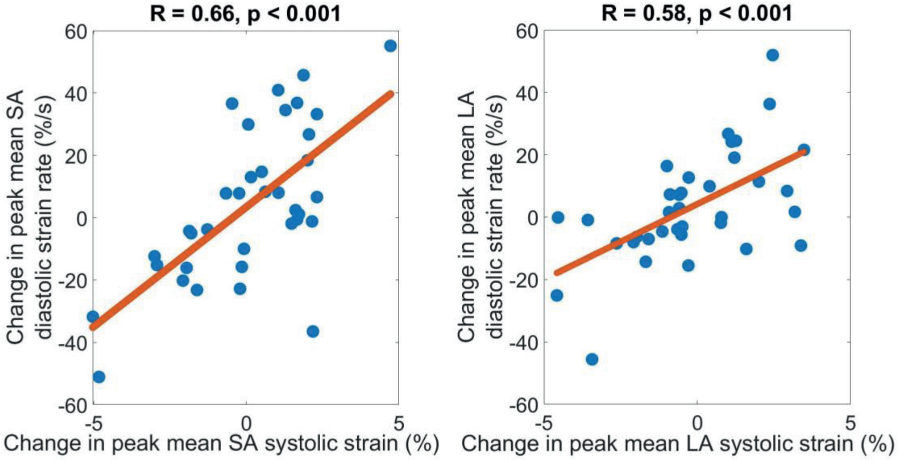

Figure 14: Correlations between the changes in peak mean systolic strain and peak mean diastolic strain rate in short-axis (SA) (left) and long-axis (LA) (right) directions in the entire study population (n = 39) (Study I).

Study III showed significant correlations in patients with hereditary gelsolin amyloidosis between peak LV longitudinal strain and mean myocardial T1 and ECV ($p < 0.04$). The correlation was most significant in the basal plane ($p < 0.01$, Figure 16). LV longitudinal strain also correlated with apical rotation and LV torsion ($p < 0.02$), with weaker longitudinal strain resulting on average in decreased rotation and lower torsion. In circumferential and radial directions, LGE was associated with peak diastolic radial strain rate and peak diastolic circumferential strain rate. Increased LGE decreased both radial and circumferential peak diastolic strain rate.

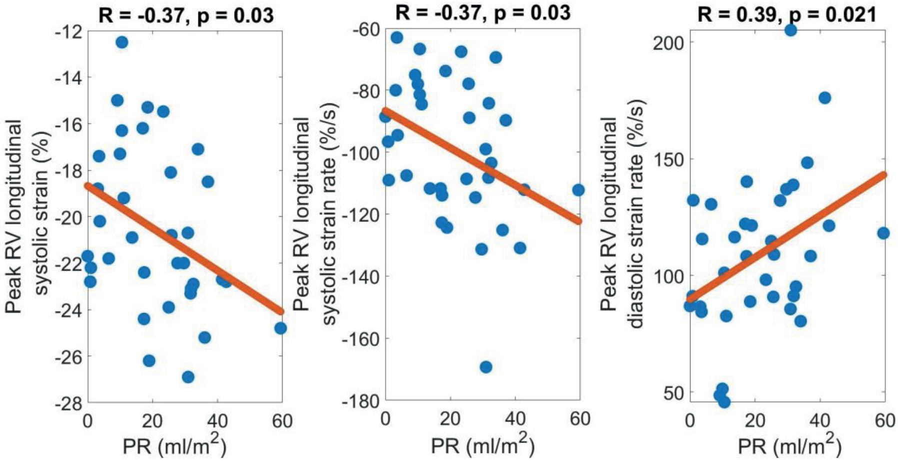

Figure 15: Correlation between pulmonary regurgitation (PR) and right ventricular peak longitudinal strain, peak systolic strain rate, and peak diastolic strain rate (Study II).

6.6 INTRA-OBSERVER VARIABILITY

Intra-observer variability of motion parameters was assessed in Studies II and IV. In Study II, the intraclass correlation coefficients of peak RV circumferential strain, peak RV longitudinal strain, peak LV circumferential strain, and peak LV longitudinal strain were 0.985 (0.97-0.99), 0.967 (0.93-0.99), 0.976 (0.90-0.99), and 0.970 (0.94-0.99), respectively. Bland-Altman plots of the same parameters and additionally peak LV radial strain are shown in Figure 17. LV peak circumferential strain showed the smallest variability, while bias was smallest in peak LV radial strain. Variability of peak RV circumferential strain and peak RV longitudinal strain did not differ significantly from corresponding LV parameters.

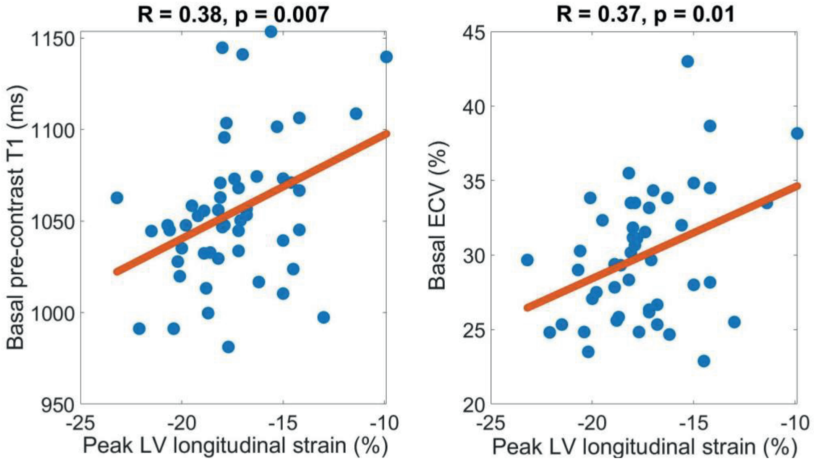

Figure 16: Correlation between peak left ventricular longitudinal strain and A) basal pre-contrast T1 and B) basal extracellular volume (ECV) (n = 50) (Study III).

In Study IV, intra-observer variability was compared between HPF and Segment in rotation of different planes and torsion (Figure 18). With both software, variability was the smallest and bias was the lowest in the analysis of basal rotation, and the highest in the torsion analysis. With HPF, 97% cases were within the 95% confidence interval of two standard deviations, compared with 92% with Segment. The bias in Segment was lower than in HPF in all motion parameters.

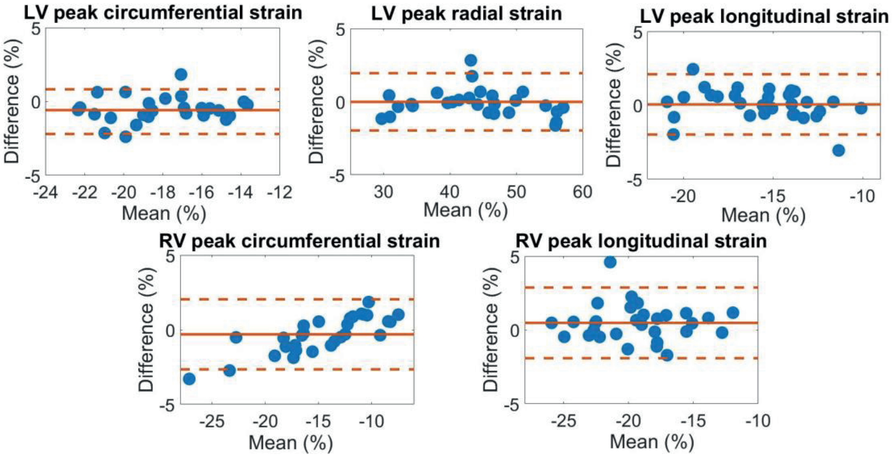

Figure 17: Intra-observer variability of LV and RV strain values with Segment (Study II).

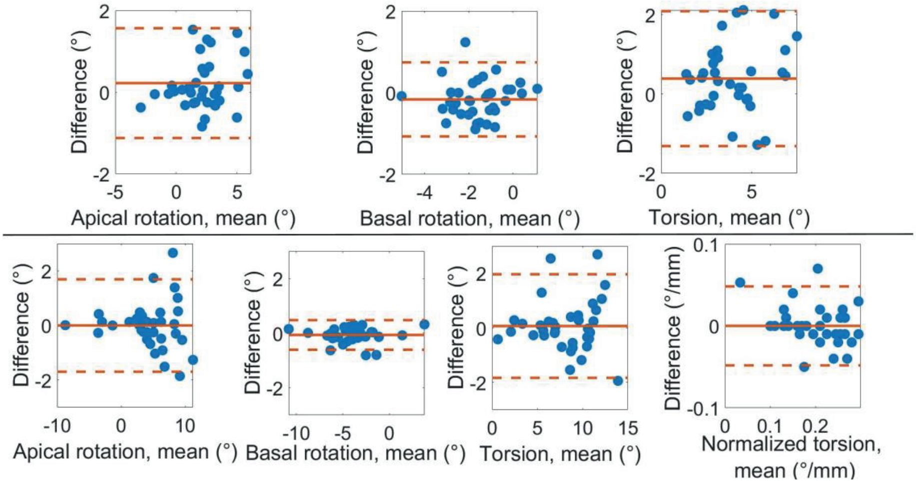

Figure 18: Intra-observer variability of rotation and torsion values analyzed with Harmonic Phase Flow (HPF, upper row) and Segment (lower row) (Study IV).

7 DISCUSSION

7.1 STUDY FINDINGS

All sub-studies of this thesis showed significant findings for myocardial motion. Study I was the first follow-up study to investigate the effects of medical treatment on myocardial motion in RA, analyzed with CMR tagging. Significant improvement in the diastolic strain rate of early RA patients was detected, focused on the anterior mid-ventricular segment. Peak mean systolic strain did not change significantly in either of the study groups, however, changes in peak mean systolic strain values correlated with changes in peak mean diastolic strain rate. Myocardial involvement and specifically diastolic dysfunction have been previously reported in RA patients free of other cardiovascular diseases [100-102]. The disease activity score of RA decreased in early RA patients during the follow-up period and was associated with changes in peak mean diastolic strain rate (Figure 10). Chronic RA patients, with a mean active disease duration of 17.3 years, showed no improvement in disease activity or strain parameters. Changes in peak diastolic strain and peak systolic strain of the entire study group showed a significant correlation (Figure 11), supporting the fact that systole and diastole are closely interdependent [103]. Changes in T1 relaxation times and LGE were not associated with changes in strain values. The study concluded that diastolic myocardial function is affected by RA and early treatment of RA targeting remission can maintain diastolic function and improve myocardial function.

Study II investigated primarily RV strain in adolescent TOF patients and presented an RV compensation mechanism in TOF patients with severe PR, where RV longitudinal strain was increased with an increasing amount of PR. Similar findings have not been observed in previous studies in adult patients with TOF [104, 105]. RV circumferential strain increased gradually from base to apex in TOF patients, contrary to healthy controls. Different cardiac planes functioned more uniformly in healthy controls, while the increase in peak RV circumferential strain from base to apex was significant in TOF patients. The observation of delayed timing of peak RV circumferential and longitudinal values (Figure 8) is consistent with right bundle branch block common after TOF repair [106]. LV function was well preserved in adolescents with TOF.

Study III was the first to characterize myocardial tissue in patients with hereditary gelsolin amyloidosis with CMR. Common to other cardiac amyloidosis, LV volumes and EF were preserved, with slightly increased LV wall thickness [107]. Myocardial tissue changes were mainly located in the basal plane of the LV. SA motion of single segments was observed to be diminished relative to other segments of the same cardiac plane. Both basal T1 relaxation times and basal LGE were associated with different motion parameters. Effects of hereditary gelsolin amyloidosis were shown to differ from the more common light-chain and familial myocardial amyloidosis.

Finally, Study IV compared harmonic phase and non-rigid registration-based analysis techniques in the analysis of systolic rotation and torsion and found that absolute rotation and torsion values differed significantly between Harmonic Phase Flow and Segment software in patients with HCM. Both software could be used reliably for systolic rotation and torsion analysis, but the study concluded that software specific reference values are required when comparing absolute motion values between individuals.

Quantitative regional assessment of myocardial motion can add incremental information that may help to develop new treatment paths in cardiac disorders. A widely adopted approach for strain analysis is to quantify mean values of ventricles; reporting planar or segmental values is not as well established. Regional strain is slowly gaining wider acceptance, and regional strain has even been recently argued to outperform the conventional LGE in RV scar detection [108]. The RV wall is thinner than LV wall, and LGE is harder to quantify. Strain, however, is easier to quantify as the endocardial border of the RV is clearly visualized in cine images. The present work argues that local motion analysis is a valuable addition to global values. Myocardial motion parameters are most valuable when analyzed with other patient characteristics [109, 110]. In this work, motion was related to disease activity scores (Study I), heart valve function (Study II) and LGE, T1, and ECV maps (Study III). The correlations detected between motion parameters and other patient parameters ranged from (±) 0.37 to 0.46, indicating weak associations between the parameters [111].

7.2 METHODOLOGICAL CONCERNS

There are many factors affecting the function of the heart and the value of an analyzed motion parameter. The image acquisition and analysis chain from a subject entering the MR scan room to acquiring a single numerical parameter of their myocardial motion has several phases and potential moments of misconduct. Subject state, their physical condition, and their capability of undergoing successful CMR are factors that influence the resulting CMR images. During imaging a proper ECG signal for gating and subject breath-hold for minimizing motion artifacts are required. To acquire tagging or cine images for proper motion analysis, image orientation and planes need to be selected according to recommendations. Sequence parameters such as trigger delay, gating method, field of view, and phase oversampling need to be set correctly to visualize the entire region of interest for analysis of the entire cardiac cycle. The first image frame in the tagging and cine image sequence should match end-diastole well, otherwise, the reference point for strain calculation is off, and the absolute value of peak strain is diminished. Images covering the entire heart are a combination of multiple sequences and even one failing can potentially ruin post-processing options due to insufficient image quality. The tagging pattern persists longer at 3T than at 1.5T, meaning better tag contrast [65]. The persistence of the tagging pattern mainly affects the analysis of diastolic strain, as the tagging pattern is created immediately before systolic cine acquisition. However, the 1-1 SPAMM tagging sequence used in Studies I and III with modern MR systems is much faster to complete than during the early 21st century. No significant difference in strain between patients imaged at 1.5T and 3T due to tag persistence was observed in Study I. CMR imaging at 3T has the benefit of a higher signal-to-noise ratio and the capability of using multi-channel excitation. There are challenges, however, with increased inhomogeneities of the RF excitation field, increased incorrect T-wave triggering, and artifacts due to tissue susceptibility in the common SSFP cine images [112]. CMR image quality is not always sufficient at 1.5T either. In Study I, basal and apical tagging images were discarded entirely due to poor image quality. Additionally, some of the basal tagging slices included parts of the LV outflow tract; in these slices, the LV wall did not remain intact throughout the cardiac cycle, and thus, could not be used for segmental motion analysis. Study II involved only the analysis of cine images, which are technically simpler to acquire than tagging images. In Study III, images were acquired prospectively, and image quality could be verified immediately after acquisition. Tagging sequences were repeated if necessary. The study population of Study IV also involved a subpopulation of a larger patient cohort with successful tagging images acquired.

The definition of myocardial rotation is unambiguous; the basal plane is adopted to rotate in the negative direction, while apical rotation is positive. However, definitions for torsion differ. The torsion definition used by HPF is the simple rotational difference between apical and basal planes. This definition was used in Study IV, which was primarily concerned with comparing rotation and torsion values between HPF and Segment. To compare rotation and torsion of different-sized hearts reliably, normalization of some sort is required. Common methods include normalizing to the longitudinal distance between apical and basal slices [27]. Segment additionally uses the mean radius of the myocardial wall in the apical and basal slices [93]. This normalization, initially by Rüssel et al., has been shown to give unbiased estimates for three-dimensional torsion and should be preferred [113]. Study IV was concerned with comparing absolute rotation values between HPF and Segment, which is why torsion was not normalized for HPF.

Deformation field calculation differs between different technical solutions. It has been argued that Gabor filters may not be optimal because they unnecessarily attenuate spectral information that contributes to motion computations [114]. This could explain the significantly lower absolute values of HPF than of Segment (Study IV). HPF uses fixed Gabor filter parameters for each SA plane, based on the type of motion normal in that plane. It is uncertain how well the Gabor filter bank functions in the case of abnormal myocardial motion, although motion tracking is based on harmonic peaks of the deformed grid pattern, which are independent of the motion of the heart.

Performing motion tracking in a certain layer of the myocardium influences the strain values obtained. Deformation of the endocardial myocardium is larger than that of the epicardial myocardium [115]. Similarly, calculation of global strain is different if the measurement is performed using the entire myocardial wall length rather than the average of segmental values. Currently, most analysis software requires endocardial and epicardial segmentation in a single frame of analysis. These contours determine the region of analysis and because different operators will contour differently different strain values will result; operator experience is an important factor in measurement accuracy. The reproducibility of different strain components is also not equivalent. Solving the displacement between adjacent analysis points is challenging when the absolute distance between points becomes shorter. This is one explanation for the usually lower reliability of RS than of CS and LS [116]. It has been generally concluded that segmental strain analysis with FT is less reliable than global strain measurements [117]. In addition, two factors in software-related aspects are critically important [115]: 1) validation of each analysis software and 2) consensus reporting among software package vendors. However, to date, no clear consensus exists. Segment strain module is a CE-marked product, while HPF is an open-source tool with independent validation by the developers [28]. It is noteworthy also that deformation field calculation in Segment is done based on the entire image and not just the segmented myocardial wall [92]. Inter-institutional variance in volumetric CMR measurements has been reported to be an important source of variability, which can be reduced by consented analysis [118]. In the present work, contouring of CMR images was thus started in consensus with a radiologist (Study I) and proceeded independently by the doctoral candidate (Studies II-IV). Intra-observer variability of motion parameters was analyzed (Studies II and IV) to verify observer reliability.

Intra- and inter-observer and intra- and inter-software variability of different FT algorithms have been well recognized and have gained significant interest in the past year [115, 119, 120]. Backhaus et al. conducted a study where they analyzed the effect of a one-hour dedicated operator training on intra-observer and inter-observer variability of strain analysis with three dedicated software [120]. They found that observer experience is an important source of variance in FT-derived strain assessment and that dedicated training, even for a short period, can significantly improve reproducibility [120]. Yet, a 2020 update of the Society for Cardiovascular Magnetic Resonance Task Force consensus statement refrained from making a dedicated statement on how quantitative evaluation of LV myocardial dynamics (strain, rotation and velocity) should be performed, as research applications are still evolving [121]. Until such recommendations and standards emerge, comparison between different software solutions remains limited.

7.3 FUTURE CHALLENGES

Steps towards standardizing strain measurements have been taken. Heinke et al. proposed standardizing FT-derived LS [122]. By standardizing they meant thorough evaluation of the entire analysis chain, starting from analysis image selection and critical assessment of tracking quality throughout the cardiac cycle. They found standardization for LS measurement helps to reduce variability introduced by inconsistencies of and between observers and inter-vendor variability. It does not, however, remove the systematic inter-vendor bias due to differences in image processing algorithms [122]. FT software have no internal quality parameters to assess tracking quality; the numbers generated with FT are always observer-related. New machine learning-based automated segmentation methods of CMR cine images are emerging and the use of automatic segmentation, when deemed reliable, has the potential to diminish observer-introduced variability in myocardial motion analysis and enables the processing of large datasets in a shorter amount of time. One such method has recently been implemented in the Segment software used in this study, with a verification dataset of 1100 individuals [123]. Another recently developed method of cine segmentation aims to completely void the need for tagging images, as they are time-consuming and require extensive post-processing [124]. However, efforts have also been made in recent years to combine spatial information with spectral information for improved tagging image analysis [114]. Both tagging and FT continue to reveive research interest.

Current mainstream analysis methods can analyze the motion of both ventricles reliably; however, atrial strain is increasingly interesting and will be the focus of future studies. CMR has also been found to be a reliable tool for atrial strain analysis [125]. This poses the next challenges for reliable and repeatable measurements in quantitative myocardial motion analysis.

8 CONCLUSIONS

Quantitative analysis of regional motion in cardiovascular magnetic resonance imaging is capable of distinguishing fine differences between different sections of the heart and is a valuable tool in the follow-up and classification of different cardiac conditions. Several software solutions exist for quantitative motion analysis and software-specific reference values are required when comparing motion values of individuals. Currently, no standardization of motion measurement exists between different software solutions, which causes variability in measures between different operators and software.

REFERENCES

[1] M.A. Konstam, F.M. Abboud, Ejection Fraction: Misunderstood and Overrated (Changing the Paradigm in Categorizing Heart Failure), Circulation 135(8) (2017) 717-719.

[2] V. Delgado, L.F. Tops, R.J. van Bommel, F. van der Kley, N.A. Marsan, R.J. Klautz, M.I. Versteegh, E.R. Holman, M.J. Schalij, J.J. Bax, Strain analysis in patients with severe aortic stenosis and preserved left ventricular ejection fraction undergoing surgical valve replacement, Eur Heart J 30(24) (2009) 3037-47.

[3] E.Y. Choi, B.D. Rosen, V.R. Fernandes, R.T. Yan, K. Yoneyama, S. Donekal, A. Opdahl, A.L. Almeida, C.O. Wu, A.S. Gomes, D.A. Bluemke, J.A. Lima, Prognostic value of myocardial circumferential strain for incident heart failure and cardiovascular events in asymptomatic individuals: the Multi-Ethnic Study of Atherosclerosis, Eur Heart J 34(30) (2013) 2354-61.

[4] S. Cheng, E.L. McCabe, M.G. Larson, A.A. Merz, E. Osypiuk, B.T. Lehman, P. Stantchev, J. Aragam, S.D. Solomon, E.J. Benjamin, R.S. Vasan, Distinct Aspects of Left Ventricular Mechanical Function Are Differentially Associated With Cardiovascular Outcomes and All-Cause Mortality in the Community, J Am Heart Assoc 4(10) (2015) e002071.

[5] S.B. Malik, N. Chen, R.A. Parker, 3rd, J.Y. Hsu, Transthoracic Echocardiography: Pitfalls and Limitations as Delineated at Cardiac CT and MR Imaging, Radiographics 37(2) (2017) 383-406.

[6] R.P. Steeds, Echocardiography: frontier imaging in cardiology, Br J Radiol 84 Spec No 3 (2011) S237-45.

[7] E.A. Zerhouni, D.M. Parish, W.J. Rogers, A. Yang, E.P. Shapiro, Human heart: tagging with MR imaging--a method for noninvasive assessment of myocardial motion, Radiology 169(1) (1988) 59-63.

[8] G. Pedrizzetti, P. Claus, P.J. Kilner, E. Nagel, Principles of cardiovascular magnetic resonance feature tracking and echocardiographic speckle tracking for informed clinical use, J Cardiovasc Magn Reson 18(1) (2016) 51.

[9] A. Schuster, K.N. Hor, J.T. Kowallick, P. Beerbaum, S. Kutty, Cardiovascular Magnetic Resonance Myocardial Feature Tracking: Concepts and Clinical Applications, Circ Cardiovasc Imaging 9(4) (2016) e004077.

[10] Muscle, 2012.

[11] V.B. Sivarajan, S.M. Schwartz, J.I.E. Hoffman, Structure and Function of the Heart, Pediatric Critical Care2011, pp. 199-216.

[12] R.E. Klabunde, Cardiovascular Physiology Concepts Chapter 2 Electrical Activity of the Heart, Lippincott Williams & Wilkins, Baltimore, MD, USA, 2012.

[13] P.J. Sheth, G.H. Danton, Y. Siegel, R.E. Kardon, J.C. Infante, Jr., E. Ghersin, J.E. Fishman, Cardiac Physiology for Radiologists: Review of Relevant Physiology for Interpretation of Cardiac MR Imaging and CT, Radiographics 35(5) (2015) 1335-51.

[14] Standardization of cardiac tomographic imaging. From the Committee on Advanced Cardiac Imaging and Technology, Council on Clinical Cardiology, American Heart Association; Cardiovascular Imaging Committee, American College of Cardiology; and Board of Directors, Cardiovascular Council, Society of Nuclear Medicine, Circulation 86(1) (1992) 338-9.

[15] M.D. Cerqueira, N.J. Weissman, V. Dilsizian, A.K. Jacobs, S. Kaul, W.K. Laskey, D.J. Pennell, J.A. Rumberger, T. Ryan, M.S. Verani, S. American Heart Association Writing Group on Myocardial, I. Registration for Cardiac, Standardized myocardial segmentation and nomenclature for tomographic

imaging of the heart. A statement for healthcare professionals from the Cardiac Imaging Committee of the Council on Clinical Cardiology of the American Heart Association, Circulation 105(4) (2002) 539-42.
[16] J.A. Rumberger, T. Behrenbeck, J.R. Breen, J.E. Reed, B.J. Gersh, Nonparallel changes in global left ventricular chamber volume and muscle mass during the first year after transmural myocardial infarction in humans, J Am Coll Cardiol 21(3) (1993) 673-82.
[17] W.D. Edwards, A.J. Tajik, J.B. Seward, Standardized nomenclature and anatomic basis for regional tomographic analysis of the heart, Mayo Clin Proc 56(8) (1981) 479-97.
[18] D. Brotman, Z. Zhang, S. Sampath, Effect of through-plane motion on left ventricular rotation: a study using slice-following harmonic phase imaging, Magn Reson Med 69(5) (2013) 1421-9.
[19] R.M. Simpson, J. Keegan, D.N. Firmin, MR assessment of regional myocardial mechanics, J Magn Reson Imaging 37(3) (2013) 576-99.
[20] A. Scatteia, A. Baritussio, C. Bucciarelli-Ducci, Strain imaging using cardiac magnetic resonance, Heart Fail Rev 22(4) (2017) 465-476.
[21] C. Johnson, K. Kuyt, D. Oxborough, M. Stout, Practical tips and tricks in measuring strain, strain rate and twist for the left and right ventricles, Echo Res Pract 6(3) (2019) R87-R98.
[22] G.J. Wehner, L. Jing, C.M. Haggerty, J.D. Suever, J. Chen, S.M. Hamlet, J.A. Feindt, W. Dimitri Mojsejenko, M.A. Fogel, B.K. Fornwalt, Comparison of left ventricular strains and torsion derived from feature tracking and DENSE CMR, J Cardiovasc Magn Reson 20(1) (2018) 63.
[23] B. Liu, A.M. Dardeer, W.E. Moody, M.K. Hayer, S. Baig, A.M. Price, F. Leyva, N.C. Edwards, R.P. Steeds, Reference ranges for three-dimensional feature tracking cardiac magnetic resonance: comparison with two-dimensional methodology and relevance of age and gender, Int J Cardiovasc Imaging 34(5) (2018) 761-775.
[24] R. Tanacli, D. Hashemi, T. Lapinskas, F. Edelmann, R. Gebker, G. Pedrizzetti, A. Schuster, E. Nagel, B. Pieske, H.D. Dungen, S. Kelle, Range Variability in CMR Feature Tracking Multilayer Strain across Different Stages of Heart Failure, Sci Rep 9(1) (2019) 16478.
[25] K. Pryds, A.H. Larsen, M.S. Hansen, A.Y.K. Grondal, R.S. Tougaard, N.H. Hansson, T.S. Clemmensen, B.B. Logstrup, H. Wiggers, W.Y. Kim, H.E. Botker, R.R. Nielsen, Myocardial strain assessed by feature tracking cardiac magnetic resonance in patients with a variety of cardiovascular diseases - A comparison with echocardiography, Sci Rep 9(1) (2019) 11296.
[26] A.M. Maceira, S.K. Prasad, M. Khan, D.J. Pennell, Reference right ventricular systolic and diastolic function normalized to age, gender and body surface area from steady-state free precession cardiovascular magnetic resonance, Eur Heart J 27(23) (2006) 2879-88.
[27] A.A. Young, B.R. Cowan, Evaluation of left ventricular torsion by cardiovascular magnetic resonance, J Cardiovasc Magn Reson 14 (2012) 49.
[28] J. Garcia-Barnés, D. Gil, S. Pujadas, F. Carreras, A Variational Framework for Assessment of the Left Ventricle Motion, Math Model Nat Phenom 3(6) (2008) 76-100.
[29] J.M. Sorger, B.T. Wyman, O.P. Faris, W.C. Hunter, E.R. McVeigh, Torsion of the left ventricle during pacing with MRI tagging, J Cardiovasc Magn Reson 5(4) (2003) 521-30.
[30] M.A. Syed, S.V. Raman, O.P. Simonetti, Basic Principles of Cardiovascular MRI, 2015.
[31] Principles of Magnetic Resonance, 1990.
[32] F. Lugauer, J. Wetzl, Magnetic Resonance Imaging, in: A. Maier, S. Steidl, V. Christlein, J. Hornegger (Eds.), Medical Imaging Systems: An Introductory Guide, Cham (CH), 2018, pp. 91-118.

[33] M. Mahesh, The Essential Physics of Medical Imaging, Third Edition, Med Phys 40(7) (2013).
[34] J.R. Macfall, Physical principles of medical imaging. Perry Sprawls, Jr, PhD, FACR Gaithersburg, Md: Aspen Publishers, 1993. S69.00; pp 656; approximately 400 illustrations, Journal of Magnetic Resonance Imaging 4(3) (1994) 258-258.
[35] R. Krishnamurthy, B. Cheong, R. Muthupillai, Tools for cardiovascular magnetic resonance imaging, Cardiovasc Diagn Ther 4(2) (2014) 104-25.
[36] Y. Wang, S.J. Riederer, R.L. Ehman, Respiratory motion of the heart: kinematics and the implications for the spatial resolution in coronary imaging, Magn Reson Med 33(5) (1995) 713-9.
[37] P. Lanzer, C. Barta, E.H. Botvinick, H.U. Wiesendanger, G. Modin, C.B. Higgins, ECG-synchronized cardiac MR imaging: method and evaluation, Radiology 155(3) (1985) 681-6.
[38] D.W. McRobbie, E.A. Moore, M.J. Graves, MRI from Picture to Proton, 2 ed., Cambridge University Press 2017.
[39] A.N. Shetty, Suppression of radiofrequency interference in cardiac gated MRI: a simple design, Magn Reson Med 8(1) (1988) 84-8.
[40] A.A. Damji, R.E. Snyder, D.C. Ellinger, F.X. Witkowski, P.S. Allen, RF interference suppression in a cardiac synchronization system operating in a high magnetic field NMR imaging system, Magn Reson Imaging 6(6) (1988) 637-40.
[41] M.S. Nacif, A. Zavodni, N. Kawel, E.Y. Choi, J.A. Lima, D.A. Bluemke, Cardiac magnetic resonance imaging and its electrocardiographs (ECG): tips and tricks, Int J Cardiovasc Imaging 28(6) (2012) 1465-75.
[42] S.B. Reeder, A.Z. Faranesh, Ultrafast pulse sequence techniques for cardiac magnetic resonance imaging, Top Magn Reson Imaging 11(6) (2000) 312-30.
[43] M. Loecher, O. Wieben, k-Space, Basic Principles of Cardiovascular MRI2015, pp. 13-23.
[44] V. Dilsizian, G.M. Pohost, Cardiac CT, PET & MR, 2019.
[45] S.J. Berkowitz, R. Macedo, A.A. Malayeri, S.M. Shea, C.H. Lorenz, H. Calkins, J. Vogel-Claussen, H. Tandri, D.A. Bluemke, Axial black blood turbo spin echo imaging of the right ventricle, Magn Reson Med 61(2) (2009) 307-14.
[46] J.L. Fleckenstein, B.T. Archer, B.A. Barker, J.T. Vaughan, R.W. Parkey, R.M. Peshock, Fast short-tau inversion-recovery MR imaging, Radiology 179(2) (1991) 499-504.
[47] A.D. Piersson, Essentials of cardiac MRI in clinical practice, Journal of Cardiovascular Magnetic Resonance 18(S1) (2016).
[48] C.M. Kramer, J. Barkhausen, C. Bucciarelli-Ducci, S.D. Flamm, R.J. Kim, E. Nagel, Standardized cardiovascular magnetic resonance imaging (CMR) protocols: 2020 update, J Cardiovasc Magn Reson 22(1) (2020) 17.
[49] P.F. Ferreira, P.D. Gatehouse, R.H. Mohiaddin, D.N. Firmin, Cardiovascular magnetic resonance artefacts, J Cardiovasc Magn Reson 15 (2013) 41.
[50] J.P. Ridgway, Cardiovascular magnetic resonance physics for clinicians: part I, J Cardiovasc Magn Reson 12 (2010) 71.
[51] S. Plein, T.N. Bloomer, J.P. Ridgway, T.R. Jones, G.J. Bainbridge, M.U. Sivananthan, Steady-state free precession magnetic resonance imaging of the heart: comparison with segmented k-space gradient-echo imaging, J Magn Reson Imaging 14(3) (2001) 230-6.
[52] J.C. Carr, O. Simonetti, J. Bundy, D. Li, S. Pereles, J.P. Finn, Cine MR angiography of the heart with segmented true fast imaging with steady-state precession, Radiology 219(3) (2001) 828-34.

[53] K. Scheffler, S. Lehnhardt, Principles and applications of balanced SSFP techniques, Eur Radiol 13(11) (2003) 2409-18.
[54] H. Sakuma, N. Fujita, T.K. Foo, G.R. Caputo, S.J. Nelson, J. Hartiala, A. Shimakawa, C.B. Higgins, Evaluation of left ventricular volume and mass with breath-hold cine MR imaging, Radiology 188(2) (1993) 377-80.
[55] D.T. Ginat, M.W. Fong, D.J. Tuttle, S.K. Hobbs, R.C. Vyas, Cardiac imaging: Part 1, MR pulse sequences, imaging planes, and basic anatomy, AJR Am J Roentgenol 197(4) (2011) 808-15.
[56] G.W. Lenz, E.M. Haacke, R.D. White, Retrospective cardiac gating: a review of technical aspects and future directions, Magn Reson Imaging 7(5) (1989) 445-55.
[57] S.E. Fischer, G.C. McKinnon, M.B. Scheidegger, W. Prins, D. Meier, P. Boesiger, True myocardial motion tracking, Magn Reson Med 31(4) (1994) 401-13.
[58] M. Doyle, E.G. Walsh, R.E. Foster, G.M. Pohost, Common k-space acquisition: a method to improve myocardial grid-tag contrast, Magn Reson Med 37(5) (1997) 754-63.
[59] J.R. Liao, J.M. Pauly, T.J. Brosnan, N.J. Pelc, Reduction of motion artifacts in cine MRI using variable-density spiral trajectories, Magn Reson Med 37(4) (1997) 569-75.
[60] L. Axel, L. Dougherty, MR Imaging of Motion with Spatial Modulation of Magnetization, Radiology 171 (1989) 841-845.
[61] E.-S. Ibrahim, Myocardial tagging by Cardiovascular Magnetic Resonance: evolution of techniques-pulse sequences, analysis, algoritms, and applications, J Cardiovasc Magn Reson 13(36) (2011).
[62] A. Bazille, M.A. Guttman, E.R. McVeigh, E.A. Zerhouni, Impact of semiautomated versus manual image segmentation errors on myocardial strain calculation by magnetic resonance tagging, Invest Radiol 29(4) (1994) 427-33.
[63] S.B. Yeon, N. Reichek, B.A. Tallant, J.A. Lima, L.P. Calhoun, N.R. Clark, E.A. Hoffman, K.K. Ho, L. Axel, Validation of in vivo myocardial strain measurement by magnetic resonance tagging with sonomicrometry, J Am Coll Cardiol 38(2) (2001) 555-61.
[64] L. Axel, L. Dougherty, Heart wall motion: improved method of spatial modulation of magnetization for MR imaging, Radiology 172(2) (1989) 349-50.
[65] V.U. Valeti, W. Chun, D.D. Potter, P.A. Araoz, K.P. McGee, J.F. Glockner, T.F. Christian, Myocardial tagging and strain analysis at 3 Tesla: comparison with 1.5 Tesla imaging, J Magn Reson Imaging 23(4) (2006) 477-80.
[66] L. Axel, Biomechanical dynamics of the heart with MRI, Annu Rev Biomed Eng 4 (2002) 321-47.
[67] F. Carreras, J. Garcia-Barnes, D. Gil, S. Pujadas, C.H. Li, R. Suarez-Arias, R. Leta, X. Alomar, M. Ballester, G. Pons-Llado, Left ventricular torsion and longitudinal shortening: two fundamental components of myocardial mechanics assessed by tagged cine-MRI in normal subjects, Int J Cardiovasc Imaging 28(2) (2012) 273-84.
[68] M.Y. Jeung, P. Germain, P. Croisille, S. El ghannudi, C. Roy, A. Gangi, Myocardial tagging with MR imaging: overview of normal and pathologic findings, Radiographics 32(5) (2012) 1381-98.
[69] Y. Notomi, R.M. Setser, T. Shiota, M.G. Marting-Miklovic, J.A. Weaver, Z.B. Popovic, H. Yamada, N.L. Greenberg, R.D. White, J.D. Thomas, Assessment of Left Ventriucal Torsion Deformation by Dopler Tissue Imaging: Validation Study With Tagged Magnetic Resonance Imaging, Circulation 111 (2005) 1141-1147.
[70] Handbook of Medical Image Processing and Analysis, 2009.

[71] C. Xu, J.J. Pilla, G. Isaac, J.H. Gorman, 3rd, A.S. Blom, R.C. Gorman, Z. Ling, L. Dougherty, Deformation analysis of 3D tagged cardiac images using an optical flow method, J Cardiovasc Magn Reson 12 (2010) 19.
[72] J.L. Prince, E.R. McVeigh, Motion estimation from tagged MR image sequences, IEEE Trans Med Imaging 11(2) (1992) 238-49.
[73] L. Dougherty, J.C. Asmuth, A.S. Blom, L. Axel, R. Kumar, Validation of an optical flow method for tag displacement estimation, IEEE Trans Med Imaging 18(4) (1999) 359-63.
[74] N.F. Osman, W.S. Kerwin, E.R. McVeigh, J.L. Prince, Cardiac Motion Tracking Using CINE Harmonic Phase (HARP) Magnetic Resonance Imaging Magn Reson Med 42(6) (1999) 1048-1060.
[75] N.F. Osman, E.R. McVeigh, J.L. Prince, Imaging Heart motion Using Harmonic Phase MRI, IEEE Trans Med Im 19(3) (2000) 186-202.
[76] A.A. Amini, Y. Chen, R.W. Curwen, V. Mani, J. Sun, Coupled B-snake grids and constrained thin-plate splines for analysis of 2-D tissue deformations from tagged MRI, IEEE Trans Med Imaging 17(3) (1998) 344-56.
[77] N. Rougon, C. Petitjean, F. Preteux, P. Cluzel, P. Grenier, A non-rigid registration approach for quantifying myocardial contraction in tagged MRI using generalized information measures, Med Image Anal 9(4) (2005) 353-75.
[78] R. Chandrashekara, R.H. Mohiaddin, D. Rueckert, Analysis of 3-D myocardial motion in tagged MR images using nonrigid image registration, IEEE Trans Med Imaging 23(10) (2004) 1245-50.
[79] J. Garcia-Barnés, D. Gil, J. Barajas, F. Carreras, S. Pujadas, P. Radeva, Characterization of Ventricular Torsion in Healthy Subjects Using Gabor Filters and a Variational Framework, Comput Cardiol 33 (2006) 887-890.
[80] A. Andaluz, F. Carreras, C. Santa Marta, D. Gil, Myocardial torsion estimation with tagged-MRI in the Osirix platform, ISBI Workshop on Open Source Medical Image Analysis Software, IEEE, 2012.
[81] S. Moon-Ho Song, S. Napel, N.J. Pelc, G.H. Glover, Phase unwrapping of MR phase images using Poisson equation, IEEE Trans Image Process 4(5) (1995) 667-76.
[82] A. Montillo, D. Metaxas, L. Axel, Extracting tissue deformation using Gabor filter banks, Proc SPIE Int Soc Opt Eng 5369 (2004).
[83] N.F. Osman, J.L. Prince, Motion estimation from tagged MR images using angle images, Int Conf Imag Proc, Comp Soc Press, Chicago, 1998, pp. 704-708.
[84] D. Rueckert, L.I. Sonoda, C. Hayes, D.L. Hill, M.O. Leach, D.J. Hawkes, Nonrigid registration using free-form deformations: application to breast MR images, IEEE Trans Med Imaging 18(8) (1999) 712-21.
[85] E. Oubel, M. De Craene, A.O. Hero, A. Pourmorteza, M. Huguet, G. Avegliano, B.H. Bijnens, A.F. Frangi, Cardiac motion estimation by joint alignment of tagged MRI sequences, Med Image Anal 16(1) (2012) 339-50.
[86] R.M. Chandrashekara, R., D. Rueckert, Cardiac motion tracking in tagged MR images using a 4D B-spline motion model and nonrigid image registration, 2004 2nd IEEE International Symposium on Biomedical Imaging: Nano to Macro, IEEE, Arlington, VA, USA, USA 2004.
[87] E. Heiberg, J. Sjögren, M. Ugander, M. Carlsson, H. Engblom, H. Arheden, Desing and Validation of Segment - a Freely Available Software for Cardiovascular Image Analysis, BMC Medical Imaging 10(1) (2010).
[88] P. Morais, B. Heyde, D. Barbosa, S. Queirós, P. Claus, J. D'Hooge, Cardiac motion and deformation estimation from tagged MRI sequences using temporal coherent image registration framework, Proceedings of the meeting on Functional Imaging and Modelling of the Heart (FIMH), Lecture notes in Computer Science vol 7945, London, 2013.

[89] B. Zitová, J. Flusser, Image registration methods: a survey, Image and Vision Computing 21(11) (2003) 977-1000.

[90] J. Kybic, M. Unser, Fast parametric elastic image registration, IEEE Trans Image Process 12(11) (2003) 1427-42.

[91] C. Ozturk, E.R. McVeigh, Four-dimensional B-spline based motion analysis of tagged MR images: introduction and in vivo validation, Phys Med Biol 45(6) (2000) 1683-702.

[92] P. Morais, A. Marchi, J.A. Bogaert, T. Dresselaers, B. Heyde, J. D'Hooge, J. Bogaert, Cardiovascular magnetic resonance myocardial feature tracking using a non-rigid, elastic image registration algorithm: assessment of variability in a real-life clinical setting, J Cardiovasc Magn Reson 19(1) (2017) 24.

[93] Segment - Technical Manual, 2020. http://medviso.com/documents/segment/techmanual.pdf. (Accessed Aug 11 2020).

[94] K.N. Hor, R. Baumann, G. Pedrizzetti, G. Tonti, W.M. Gottliebson, M. Taylor, D.W. Benson, W. Mazur, Magnetic resonance derived myocardial strain assessment using feature tracking, J Vis Exp (48) (2011).

[95] J.L. Barron, D.J. Fleet, S.S. Beauchemin, Performance of optical flow techniques, International Journal of Computer Vision 12(1) (1994) 43-77.

[96] M. Tarkiainen, P. Sipola, M. Jalanko, T. Helio, M. Laine, V. Jarvinen, K. Hayrinen, K. Lauerma, J. Kuusisto, Cardiovascular magnetic resonance of mitral valve length in hypertrophic cardiomyopathy, J Cardiovasc Magn Reson 18(1) (2016) 33.

[97] P. Jaaskelainen, T. Helio, K. Aalto-Setala, M. Kaartinen, E. Ilveskoski, L. Hamalainen, J. Melin, M.S. Nieminen, M. Laakso, J. Kuusisto, H.C.M.s.g. Fin, H. Kervinen, J. Mustonen, J. Juvonen, M. Niemi, P. Uusimaa, M. Huttunen, M. Kotila, M. Pietila, Two founder mutations in the alpha-tropomyosin and the cardiac myosin-binding protein C genes are common causes of hypertrophic cardiomyopathy in the Finnish population, Ann Med 45(1) (2013) 85-90.

[98] R.J. Taylor, W.E. Moody, F. Umar, N.C. Edwards, T.J. Taylor, B. Stegemann, J.N. Townend, K.N. Hor, R.P. Steeds, W. Mazur, F. Leyva, Myocardial strain measurement with feature-tracking cardiovascular magnetic resonance: normal values, Eur Heart J Cardiovasc Imaging 16(8) (2015) 871-81.

[99] P. Haaf, P. Garg, D.R. Messroghli, D.A. Broadbent, J.P. Greenwood, S. Plein, Cardiac T1 Mapping and Extracellular Volume (ECV) in clinical practice: a comprehensive review, J Cardiovasc Magn Reson 18(1) (2016) 89.

[100] M. Holmstrom, R. Koivuniemi, K. Korpi, T. Kaasalainen, M. Laine, A. Kuuliala, M. Leirisalo-Repo, M. Kupari, S. Kivisto, Cardiac magnetic resonance imaging reveals frequent myocardial involvement and dysfunction in active rheumatoid arthritis, Clin Exp Rheumatol 34(3) (2016) 416-23.

[101] Y. Kobayashi, J.T. Giles, M. Hirano, I. Yokoe, Y. Nakajima, J.M. Bathon, J.A. Lima, H. Kobayashi, Assessment of myocardial abnormalities in rheumatoid arthritis using a comprehensive cardiac magnetic resonance approach: a pilot study, Arthritis Res Ther 12(5) (2010) R171.

[102] K.P. Liang, E. Myasoedova, C.S. Crowson, J.M. Davis, V.L. Roger, B.L. Karon, D.D. Borgeson, T.M. Therneau, R.J. Rodeheffer, S.E. Gabriel, Increased prevalence of diastolic dysfunction in rheumatoid arthritis, Ann Rheum Dis 69(9) (2010) 1665-70.

[103] D.P. Leong, C.G.D. Pasquele, J.B. Selvanayagam, Heart Failure With Normal Ejection Fraction: The Comlementary Roles of Echocardiography and CMR Imaging, JACC Cardiovasc Imaging 3(4) (2010).

[104] L. Jing, C.M. Haggerty, J.D. Suever, S. Alhadad, A. Prakash, F. Cecchin, O. Skrinjar, T. Geva, A.J. Powell, B.K. Fornwalt, Patients with repaired

tetralogy of Fallot suffer from intra- and inter-ventricular cardiac dyssynchrony: a cardiac magnetic resonance study, Eur Heart J Cardiovasc Imaging 15(12) (2014) 1333-43.

[105] L. Jing, G.J. Wehner, J.D. Suever, R.J. Charnigo, S. Alhadad, E. Stearns, D. Mojsejenko, C.M. Haggerty, K. Hickey, A.M. Valente, T. Geva, A.J. Powell, B.K. Fornwalt, Left and right ventricular dyssynchrony and strains from cardiovascular magnetic resonance feature tracking do not predict deterioration of ventricular function in patients with repaired tetralogy of Fallot, J Cardiovasc Magn Reson 18(1) (2016) 49.

[106] L.N. Horowitz, M.B. Simson, J.F. Spear, M.E. Josephson, E.N. Moore, J.A. Alexander, J.A. Kastor, L.H. Edmunds, Jr., The mechanism of apparent right bundle branch block after transatrial repair of tetralogy of Fallot, Circulation 59(6) (1979) 1241-52.

[107] A. Martinez-Naharro, T.A. Treibel, A. Abdel-Gadir, H. Bulluck, G. Zumbo, D.S. Knight, T. Kotecha, R. Francis, D.F. Hutt, T. Rezk, S. Rosmini, C.C. Quarta, C.J. Whelan, P. Kellman, J.D. Gillmore, J.C. Moon, P.N. Hawkins, M. Fontana, Magnetic Resonance in Transthyretin Cardiac Amyloidosis, J Am Coll Cardiol 70(4) (2017) 466-477.

[108] T. Zghaib, M.A. Ghasabeh, F.R. Assis, J. Chrispin, A. Keramati, S. Misra, R. Berger, H. Calkins, I. Kamel, S. Nazarian, S. Zimmerman, H. Tandri, Regional Strain by Cardiac Magnetic Resonance Imaging Improves Detection of Right Ventricular Scar Compared With Late Gadolinium Enhancement on a Multimodality Scar Evaluation in Patients With Arrhythmogenic Right Ventricular Cardiomyopathy, Circ Cardiovasc Imaging 11(9) (2018) e007546.

[109] A.I. Nagy, A. Sahlen, A. Manouras, L. Henareh, C. da Silva, E. Gunyeli, A.A. Apor, B. Merkely, R. Winter, Combination of contrast-enhanced wall motion analysis and myocardial deformation imaging during dobutamine stress echocardiography, Eur Heart J Cardiovasc Imaging 16(1) (2015) 88-95.

[110] A.C. Ng, M. Sitges, P.N. Pham, T. Tran da, V. Delgado, M. Bertini, G. Nucifora, J. Vidaic, C. Allman, E.R. Holman, J.J. Bax, D.Y. Leung, Incremental value of 2-dimensional speckle tracking strain imaging to wall motion analysis for detection of coronary artery disease in patients undergoing dobutamine stress echocardiography, Am Heart J 158(5) (2009) 836-44.

[111] M.M. Mukaka, Statistics corner: A guide to appropriate use of correlation coefficient in medical research, Malawi Med J 24(3) (2012) 69-71.

[112] J.N. Oshinski, J.G. Delfino, P. Sharma, A.M. Gharib, R.I. Pettigrew, Cardiovascular magnetic resonance at 3.0 T: current state of the art, J Cardiovasc Magn Reson 12 (2010) 55.

[113] I.K. Russel, S.R. Tecelao, J.P. Kuijer, R.M. Heethaar, J.T. Marcus, Comparison of 2D and 3D calculation of left ventricular torsion as circumferential-longitudinal shear angle using cardiovascular magnetic resonance tagging, J Cardiovasc Magn Reson 11 (2009) 8.

[114] M. Nitzken, G.M. Beache, M. Ismail, G. Gimel'farb, A. El-Baz, Improving full-cardiac cycle strain estimation from tagged CMR by accurate modeling of 3D image appearance characteristics, The Egyptian Journal of Radiology and Nuclear Medicine 47(1) (2016) 83-94.

[115] M.S. Amzulescu, M. De Craene, H. Langet, A. Pasquet, D. Vancraeynest, A.C. Pouleur, J.L. Vanoverschelde, B.L. Gerber, Myocardial strain imaging: review of general principles, validation, and sources of discrepancies, Eur Heart J Cardiovasc Imaging 20(6) (2019) 605-619.

[116] A. Schuster, V.C. Stahnke, C. Unterberg-Buchwald, J.T. Kowallick, P. Lamata, M. Steinmetz, S. Kutty, M. Fasshauer, W. Staab, J.M. Sohns, B. Bigalke, C. Ritter, G. Hasenfuss, P. Beerbaum, J. Lotz, Cardiovascular magnetic resonance feature-tracking assessment of myocardial mechanics: Intervendor agreement and considerations regarding reproducibility, Clin Radiol 70(9) (2015) 989-98.

[117] L. Wu, T. Germans, A. Guclu, M.W. Heymans, C.P. Allaart, A.C. van Rossum, Feature tracking compared with tissue tagging measurements of segmental strain by cardiovascular magnetic resonance, J Cardiovasc Magn Reson 16(10) (2014) 10.
[118] P. Beerbaum, P. Barth, S. Kropf, S. Sarikouch, A. Kelter-Kloepping, D. Franke, M. Gutberlet, T. Kuehne, Cardiac function by MRI in congenital heart disease: impact of consensus training on interinstitutional variance, J Magn Reson Imaging 30(5) (2009) 956-66.
[119] P. Pierpaolo, S. Rolf, B.P. Manuel, C. Davide, T. Dresselaers, P. Claus, J. Bogaert, Left ventricular global myocardial strain assessment: Are CMR feature-tracking algorithms useful in the clinical setting?, Radiol Med 125(5) (2020) 444-450.
[120] S.J. Backhaus, G. Metschies, M. Billing, J.T. Kowallick, R.J. Gertz, T. Lapinskas, B. Pieske, J. Lotz, B. Bigalke, S. Kutty, G. Hasenfuss, P. Beerbaum, S. Kelle, A. Schuster, Cardiovascular magnetic resonance imaging feature tracking: Impact of training on observer performance and reproducibility, PLoS One 14(1) (2019) e0210127.
[121] J. Schulz-Menger, D.A. Bluemke, J. Bremerich, S.D. Flamm, M.A. Fogel, M.G. Friedrich, R.J. Kim, F. von Knobelsdorff-Brenkenhoff, C.M. Kramer, D.J. Pennell, S. Plein, E. Nagel, Standardized image interpretation and post-processing in cardiovascular magnetic resonance - 2020 update : Society for Cardiovascular Magnetic Resonance (SCMR): Board of Trustees Task Force on Standardized Post-Processing, J Cardiovasc Magn Reson 22(1) (2020) 19.
[122] R. Heinke, F. Pathan, M. Le, T. D'Angelo, L. Winau, C. Arendt, T.J. Vogl, A. Zeiher, E. Nagel, V.O. Puntmann, Towards standardized postprocessing of global longitudinal strain by feature tracking - OptiStrain CMR-FT study, BMC Cardiovasc Disord 19(1) (2019) 267.
[123] K. Berggren, E. Hedstrom, K. Steding Ehrenborg, M. Carlsson, H. Engblom, E. Ostenfeld, J. Jogi, D. Atar, U. Ekelund, H. Arheden, E. Heiberg, Multiple Convolutional Neural Networks for Robust Myocardial Segmentation, Svenska Sällskapet för Automatiserad Bildanalys, Helsingborg, 2020.
[124] K. Hammouda, F. Khalifa, H. Abdeltawab, A. Elnakib, G.A. Giridharan, M. Zhu, C.K. Ng, S. Dassanayaka, M. Kong, H.E. Darwish, T.M.A. Mohamed, S.P. Jones, A. El-Baz, A New Framework for Performing Cardiac Strain Analysis from Cine MRI Imaging in Mice, Sci Rep 10(1) (2020) 7725.
[125] Y. Yang, G. Yin, Y. Jiang, L. Song, S. Zhao, M. Lu, Quantification of left atrial function in patients with non-obstructive hypertrophic cardiomyopathy by cardiovascular magnetic resonance feature tracking imaging: a feasibility and reproducibility study, J Cardiovasc Magn Reson 22(1) (2020) 1.

ORIGINAL PUBLICATIONS